LOW TEMPERATURE GROWN GaAs BASED RESONANT CAVITY ENHANCED PHOTODIODES

A THESIS
SUBMITTED TO THE DEPARTMENT OF ELECTRICAL AND ELECTRONICS ENGINEERING
AND THE INSTITUTE OF ENGINEERING AND SCIENCE
OF BİLKENT UNIVERSITY
IN PARTIAL FULFILLMENT OF THE REQUIREMENTS
FOR THE DEGREE OF
MASTER OF SCIENCE

By

Bayram Bütün

I certify that I have read this thesis and that in my opinion it is fully adequate, in scope and in quality, as a dissertation for the degree of Master of Science.

____

Prof. Orhan Aytür (Supervisor)

I certify that I have read this thesis and that in my opinion it is fully adequate, in scope and in quality, as a dissertation for the degree of Master of Science.

____

Prof. Ekmel Özbay

I certify that I have read this thesis and that in my opinion it is fully adequate, in scope and in quality, as a dissertation for the degree of Master of Science.

____

Assist. Prof. Özgür Aktaş

Approved for the Institute of Engineering and Science:

____

Prof. Mehmet Baray,

Director of the Institute of Engineering and Science

Abstract

LOW TEMPERATURE GROWN GaAs BASED
RESONANT CAVITY ENHANCED PHOTODIODES

Bayram Bütün
M. S. in Electrical and Electronics Engineering
Supervisor: Prof. Orhan Aytür
January 2004

High performance photodetectors operating in the 1.3 - 1.6 μm wavelength range are vital components for long-haul optical fiber communication systems. GaAs with its mature fabrication methods is one of the most used semiconductors in photodetector technology, but with a low cut-off wavelength around 870 nm. To use GaAs at longer wavelengths, a new growth technique has been developed, in which GaAs was grown at low temperatures (LT-GaAs), so that it absorbs photons with wavelengths up to 1.7 μm.

In this work, we report the design, growth, fabrication, and characterization of GaAs-based high-speed p-i-n photodiodes operating at 1.55 μm. A LT-GaAs layer was used as the absorption layer and the photoresponse was selectively enhanced at 1.55 μm using a resonant cavity detector structure. The bottom mirror of the resonant cavity was formed by a highly reflective 15-pair GaAs/AlAs Bragg mirror. Molecular beam epitaxy was used for wafer growth, where the active LT-

GaAs layer was grown at a substrate temperature of 200 °C. The fabricated devices exhibited resonance around 1548 nm. When compared to the efficiency of a conventional single-pass detector, an enhancement factor of 7.5 was achieved. Temporal pulse-response measurements were carried out at 1.55 μm. Fast pulse responses with 30 ps pulse-width and a corresponding 3-dB bandwidth of 11.2 GHz was measured.

Keywords: GaAs, p-i-n photodiode, low temperature grown GaAs, molecular beam epitaxy, resonance cavity enhancement.

Özet

DÜŞÜK SICAKLIKTA BÜYÜTÜLMÜŞ GaAs TABANLI REZONANT KAVİTE ARTTIRIMLI FOTODİYOTLAR

Bayram Bütün
Elektrik ve Elektronik Mühendisliği Yüksek Lisans
Tez Yöneticisi: Prof. Orhan Aytür
Ocak 2004

Uzun mesafe fiber optik haberleşme sistemlerinde, 1.3-1.6 μm dalgaboyu aralığında çalışan fotodedektörler çok önemlidir. Gelişmiş üretim ve işleme teknolojisiyle GaAs, fotodedektör teknolojisinde en çok kullanılan yarıiletkenlerden biridir. Bununla birlikte, 870 nm civarinda kesilen soğurum tayfı nedeniyle yüksek dalgaboylarında kullanılamamaktadır. Yakın geçmişte, GaAs yarıiletkenini sözü geçen dalga boylarında da kullanabilmek için, yeni bir büyütme tekniği geliştirildi. Böylece yeni yapı, ışığı 1.7 μm dalgaboyuna kadar soğurabiliyor.

Bu çalışmamızda, 1.55 μm'de çalışan, yüksek hızlı, p-i-n yapısında GaAs tabanlı fotodetektörlerin tasarımı, büyütülmesi, üretimi ve karakterizasyonunu sunuyoruz. Soğuran tabaka olarak düşük sıcaklıkta büyütülmüş GaAs kullanıldı. Işığın emilimi 1.55 μm etrafındaki dar bir aralıkta, rezonant kavite yapısı

kullanılarak artırıldı. Taban aynası 15 çift GaAs/AlAs tabakasından oluşan Bragg Aynası şeklinde oluşturuldu. Tüm yapı, emilim bölgesi 200 ºC sıcaklığında olmak üzere, moleküler ışın büyütümü tekniğiyle büyütüldü. Üretilen aygıtların rezonansının 1548 nm'de olduğu görüldü. Işığın emilim bölgesinden bir defa geçtiği yapıyla karşılaştırıldığında, rezonanstan kaynaklanan yükseltim faktörünün 7.5 olduğu ölçüldü. 1.55 µm de gerçekleştirilen yüksek hız ölçümünde 11.2 GHz'e bant genişliğine karşılık gelen, 30 ps darbe tepkisi kaydedildi.

Anahtar Sözcükler: GaAs, p-i-n fotodiyot, düşük sıcaklıkta büyütülmüş GaAs, moleküler ışın büyütümü, rezonant kavite artırımı.

Acknowledgements

It is my pleasure to express my sincere gratitude to my supervisors Prof. Orhan Aytür and Prof. Ekmel Özbay. In their work and personality, I have seen endless motivation and boundless enthusiasm for science, which I will always try to have. This work would not be possible without their encouragements.

I would like to thank Assist. Prof. Özgür Aktaş for his comments and being in my thesis committee.

I am indebted to Necmi Bıyıklı, İbrahim Kimukin and Murat Güre, for they taught me (almost) everything they know about semiconductor processing and characterization.

Special thanks belong to my wife, Yeliz, for her nonstop support, and for shining a different color to my life. I dedicate this labor to her.

Contents

Abstract **i**

Özet **iii**

Acknowledgements **v**

Contents **vi**

List of Figures **viii**

List of Tables **xi**

1 Introduction **1**

2 Theory and Design **4**

2.1 P-I-N Photodiode Theory………………………………………. 6

2.1.1 Detector Operation……………………………………… 8

2.1.2 Detector Performance………………………………….. 11

2.2 Optical Multilayer Films……………………………………….. 14

2.3 Resonant Cavity Enhancement…………………………………… 17

2.3.1 Formulation…………………………………………….. 18

2.3.2 Standing Wave Effect………………………………….. 21

2.4 Design of Photodetector………………………………………... 22

2.4.1 LT-GaAs Material Properties…………………………… 22

2.4.2 Cavity Design…………………………………………… 24

3 Fabrication **29**

3.1 Molecular Beam Epitaxy ……………………………………… 29

3.2 Basic Process Steps…………………………………………….. 32
3.2.1 Wafer Cleaving and Sample Cleaning………………….. 32
3.2.2 Photolithography……………………………………... 33
3.2.3 Etching……………………………………………….. 37
3.2.4 Thin Film Coating……………………………………. 38
3.3 Device Process Steps…………………………………………... 39
3.3.1 Cavity Tuning………………………………………... 39
3.3.2 Ohmic Contact Deposition and Thermal Annealing……. 39
3.3.3 Mesa Isolation………………………………………………... 41
3.3.4 Dielectric Coating……………………………………………. 41
3.3.5 Interconnect Metallization ……………………………….... 42
3.3.6 Lift-off…………………………………………………………... 42
3.3.7 Airbridge Metal Formation……………………………….... 42
4 Measurements **51**
4.1 Current vs. Voltage Measurements…….…………………….... 51
4.2 Quantum Efficiency Measurements……………….…………….. 52
4.3 High Speed Measurements………………….………………… 57
5 Achievements and Future Directions **60**
Bibliography **62**

List of Figures

2.1 Diode structure and energy band diagram under reverse bias………… 7

2.2 Distribution of dopant-ion charges, electric field and voltage for a p-i-n photodiode under reverse bias…………………………………… 9

2.3 a) The induced current as a function of time, where photogeneration took place only at a sheet in the active region. b) Output current for a uniformly illuminated diode, where electron drift velocity is larger than the hole drift velocity…………………………………………... 12

2.4 Schematics of photodiode circuitry under reverse bias (a) and equivalent high speed model for frequency analysis (b)...……….…… 13

2.5 First building block of optical multilayer films; electric field is transferred from one side of a boundary to the other side……………... 14

2.6 Second building block of optical multilayer films: Electric field is transferred, or propagated, inside a homogeneous medium…………… 15

2.7 A general multilayer film, with electric fields before and after the stack………………………………………………………………. 16

2.8 Lateral structure of RCE photodetector ……………………………….. 19

2.9 Epitaxial structure of LT-GaAs wafer…………………………………. 26

2.10 Simulated absorption at the active region, reflectance and transmittance of the LT-GaAs wafer…………………………………... 27

2.11 Simulated absorption at the active region …………………………….. 27
2.12 Electric field distribution throughout the epitaxial structure. The point '0 nm' is the front surface of the wafer, and the area between the bold lines is the active area…………………………………..………… 28
3.1 Schematic diagram of MBE system……………………………………. 30
3.2 Scanning electron microscope image of wafer………………………… 32
3.3 Basic resist processes: a) Liftoff process for all metallization steps, b) Etch process for coatings, only at SiN_x passivation coating step, c) Etch process for ohmic and mesa etch steps ……………………….. 35
3.4 Normal PL and image reversal PL. Note to the photoresist walls in either case. Image reversal PL method makes liftoff process easier….. 36
3.5 Alignment marks and development pattern after first PL, i.e. no alignment made yet. Gray areas are photoresist. Upper right quarter of development patterns has 25 of 1 μm wide grooves separated by 1 μm. 36
3.6 Cavity tuning of a sample by etching: a) deviation in GaAs layers are -8.0% and in AlAs layers +4.0%. Absorption peak is around 1600 nm. b) after 20 nm surface etch, c) after 45 nm more surface etch, d) after 15nm more etch, and the absorption peak is at 1548nm……………….. 40
3.7 Test pattern for measuring ohmic contact resistance…………………... 41
3.8 Photodetectors with quantum efficiency mask sequence. Notice cheese-like metal surfaces of n+ ohmic contacts, which occur after RTP……………………………………………………………….. 49
3.9 Photodetectors of 20 μm x 20 μm active area, with high speed mask sequence. Left photograph is was taken after bridge metallization PL.

	Areas of bridges and top MIM capacitor layers are open and the rest is with resist. Right photograph shows the result after all of the steps are finished, and the dark square area is dielectric……………………….....	49
3.10	Lateral structure of photodetector after fabrication…………………….	50
4.1	Current vs. Voltage characteristic of different size photodetectors…….	52
4.2	Basic schematics of quantum efficiency setup…………………………	53
4.3	Quantum Efficiency of 60 µm diameter device from USA wafer……..	53
4.4	Quantum efficiency of 60 µm diameter device from Spain wafer……..	55
4.5	Quantum Efficiency of single-pass device with 150 µm diameter…….	55
4.6	Measurement and simulation of RCE and single pass devices, of 60 µm diameter. Squares: measured QE of RCE structure; circles: measured QE of single pass structure; line and dots: simulations ……..	56
4.7	Basic schematics of high-speed setup………………………………….	57
4.8	Temporal response of 30 µm device with increasing reverse bias voltage, as 1, 3, 5, 7 and 10 V…………………………………………..	59
4.9	Temporal response of a 7 µm x 7 µm device with changing optical power illumination…………………………………………………...	59

List of Tables

2.1 Comparison of the properties of LT-GaAs with undoped GaAs grown by MBE…………………………………………………….. 23

2.2 Absorption lengths of GaAs and LT-GaAs at different wavelengths, where detectors were fabricated……………………………………… 24

3.1 Evaporated metals and their thicknesses for n+ ohmic contacts……... 41

3.2 Process details for a p-i-n photodetector (standart process)……...…. 44

3.3 Process details for a p-i-n photodetector (high speed process)………. 46

4.1 Peak quantum efficiencies and figures of enhancement at resonance under different bias conditions. (The RCE device is 100 μm in diameter, and the single-pass device is 150 μm in diameter) ……….. 57

"I can live with doubt and uncertainty and not knowing - I think it's much more interesting to live not knowing than to have answers that might be wrong. I have approximate answers and possible beliefs and different degrees of certainty about different things, but I'm not absolutely sure of anything, and many things I don't know anything about, such as whether it means anything to ask why we're here, and what the question might mean. I might think about it a little bit, but if I can't figure it out, then I go on to something else. But I don't have to know an answer...
I don't feel frightened by not knowing things, by being lost in the mysterious universe without having any purpose, which is the way it really is, as far as I can tell, possibly. It doesn't frighten me."

R. P. Feynman

Chapter 1
Introduction

"Photodetectors are the forerunners of any frontier in optoelectronics. When an unusual spectral change or a new frequency band is explored, photodetectors are the first to establish a tool for handling the optical signal. Then, optical components and laser sources follow. Thus, the excitement of the discovery comes more frequently with photodetectors than with the other optoelectronic devices [1]."

The birth of photodetectors can be dated back to late 19th century, when photoconductivity in selenium was observed. Later in the last century, with the discoveries of the photoelectric effect, photoelectric vacuum tubes, photomultiplier, semiconductor devices and many more phenomena, we witness a very rapid advancement in communication technology. Usage of detectors in space missions and space telescopes, for example, may be a validation of above comment. It is apparent that the above comment is not an exaggeration.

Today, we are living in the era of communication. Except the transfer of information via wireless networks, such as cellular phone and satellite communication, all of information is carried through optical fibers. The research efforts in optoelectronics are fully devoted toward the exploitation of the fiber bandwidth, which can be possible with high performance components.

Photodetectors are the last part of the fiber optic channel; after lasers, modulators and fiber cables. With the photodetector, we convert optical signal to the electrical signal that can be processed more easily than the optical signal, at least today. Since everything is getting smaller and faster, photodetectors are getting smaller and faster too. This reduction in size results additional concerns, and we face with several tradeoffs [2].

Semiconductor based photodiodes demonstrate excellent capabilities to overcome these tradeoffs, and among the different elemental and compound semiconductors, GaAs is the most investigated semiconductor for photodetection [3].

High-performance photodetectors operating in the 1.3-1.6 μm range are vital components for long-haul optical fiber communication systems [4], after developments in wavelength division multiplexing research and Erbium doped fiber amplifiers. However, conventional GaAs-based photodetectors can only operate in the first optical communication window (λ ~850 nm) due to the low cut-off wavelength. To overcome this limitation and to use GaAs-based detectors in the 1.3-1.6 μm wavelength region, two detector structures were offered: Schottky-barrier internal photo-emission photodetectors [5] and Low Temperature Grown GaAs (LT-GaAs) based photodetectors [6].

It was shown that LT-GaAs was able to absorb long-wavelength signals due to mid-gap defects or As precipitates [7, 8]. Moreover, sub-picosecond carrier trapping time in LT-GaAs was also demonstrated [9-11]. Combining these two unique properties, LT-GaAs-based high-speed photodetectors operating in the 1.3-1.6 μm range have been reported [7, 12, 13]. Using its low carrier trapping time, photodetectors operated around 800 nm with record bandwidths up to 560 GHz [14-18]; switches for up to 20 Gb/sec clock rates [8] and research efforts for all-optical switching [9, 11, 19-23] have been reported.

The long-wavelength (below-bandgap) absorption coefficient of LT-GaAs is much smaller than the inter-band absorption coefficient [22]. This leads to poor efficiency performance with conventional single-pass vertical detector structures. To overcome the problem of low efficiency, edge-coupled LT-GaAs waveguide photodetectors were proposed and successfully demonstrated [14]. Another method for improving the device efficiency is to use a resonant cavity enhanced (RCE) detector structure. With this structure, the detector efficiency is selectively enhanced at the resonance wavelengths of the resonant cavity [24]. Several groups have reported high-performance photodetectors using RCE detection scheme [5, 25-30]. This technique can also be used to improve the efficiency performance of LT-GaAs-based photodetectors. Previously, GaAs-based RCE Schottky-barrier internal photoemission photodetector operating at 1.3 μm has been demonstrated [31].

In this work, we designed, fabricated and demonstrated the first LT-GaAs based RCE p-i-n photodetector with high speed operation at 1.55 μm.

We presented the theory of p-i-n photodiodes in Chapter 2, together with the examination of carrier transport. Then, we explained the simulation method of diodes, namely the transfer matrix method (TMM) and RCE effect. In the last part, we demonstrated the LT-GaAs material properties and design of LT-GaAs based p-i-n photodiode.

Chapter 3 was devoted to the gowth and the fabrication of the detector structures. This chapter starts with the description of molecular beam epitaxial (MBE) growth of the wafers, which were actually grown in other research centers in USA and Spain. We then, present the fabrication process we have developed in our university.

The characterization results are presented in Chapter 4. These include current vs. voltage (IV) measurements, quantum efficiency and high-speed measurements.

Our research effort is summarized in Chapter 5. Possible reasons for not being able to achieve the best results are explained and our future research plan is subsequently described.

Chapter 2

Theory and Design

In this chapter, we first present the operation of a p-i-n photodiode. Then the transfer matrix method (TMM), which is used in almost all the stages of fabrication and measurements, will be explained. In the last section, the design of the photodetector together with its material properties will be described.

Photodetectors can be broadly defined as devices that measure optical power by converting the energy of the absorbed photons into a measurable form [1, 32]. Generally, output of the detector is an electrical signal in response to or as a replica of the input light signal [1]. They are the key elements in virtually any optoelectronic system and application, paralleling in importance to the role of sources [1]. Detectors can be classified according to the generation of electrical output signal as thermal detectors and photoelectric detectors. Thermal detectors operate using the heat that is generated by the photons absorbed by the detector material. Since temperature change requires much longer times as compared to the absorption effect and the involvement of phonon interactions, this kind of detectors, such as thermocouples, bolometers, and pyroelectrics are rather inefficient and relatively slow. The operation of photoelectric detectors is based on the photoelectric effect, in which the absorption of photons by the material, results in mobile charge carriers, namely electrons and holes. Under the effect of an electric field, generated by the

material itself, or by an outside bias voltage, these carriers are transported and a measurable electric current is generated. In other words, the photodetection process can be schematized by the following sequence [1]:

- Absorption of photons in the material with the generation of charge carriers,
- Drift of charge carriers under a suitable internal electric field,
- Collection of charge carriers at the electric contacts of the device.

2.1 P-I-N Photodiode Theory

A photodiode is basically a p-n junction operated under reverse bias, and a p-i-n photodiode is a member of the diode family that consists of a p-n junction diode, p-i-n diode, metal-semiconductor diode, and heterojunction diode [33]. This classification is based on the junction types that form the diode.

The p-i-n photodiode is one of the most common photodetectors, because the depletion region thickness can be engineered to optimize the quantum efficiency (QE) and frequency response. Figure 2.1 shows the structure of a basic diode and energy-band diagram. An intrinsic layer is stacked between the p and n layers. If the intrinsic layer is depleted completely with reverse bias, photogenerated carriers are separated by the electric field and contribute to the external current if they can reach to the ohmic contacts, which is called drift current. The speed of the devices, here, depends on the transportation of the carriers from the far edge, n contact for holes and p side for electrons, for example. However, if the light is also absorbed inside the p and n regions, another component comes into the picture, namely diffusion current. Diffusion current may slow down the device considerably, depending on the lifetime of the photogenerated carriers, with tens of nanoseconds [33, 34] in GaAs, for example. Allowing absorption only in the i-region, by heterojunctions, can

eliminate this drawback. So there is no diffusion current contributing to the output current. Therefore, with heterojunction p-i-n photodiodes, high efficiency and high speeds can be achieved at the same time.

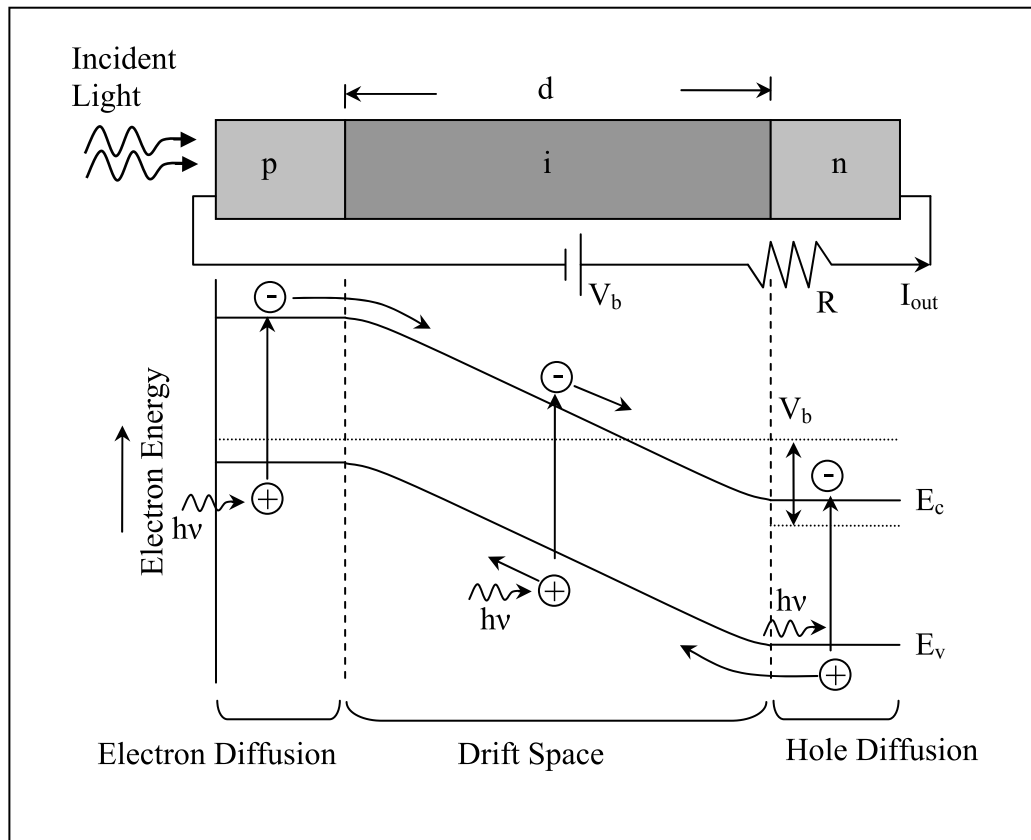

Figure 2.1: Diode structure and energy band diagram under reverse bias.

The advantages of the p-i-n photodiode over the p-n junctions are as follows: [1]

- The thickness of the absorption region is determined by the geometry of the device, independently from V_b, which has very little effect on the

spectral response. Therefore, even with low bias, a good efficiency can be obtained.

- With the depletion region in i-region that is much longer than the depletion regions at p+ and n+, as in Fig. 2.2, the diffusion contributions can be kept small, which can be achieved via doping concentrations. Thus, we can obtain the frequency response independent of λ.
- Since the electric field, E, is constant in the active layer, the intrinsic speed of response (i.e. overall drift time for photogenerated carriers) is optimized.

2.1.1 Detector Operation

When reverse bias is applied to the device, as shown in Fig. 2.2, an intrinsic layer will have a continuous and constant electric field. When an optical input at a wavelength λ (corresponding to a photon energy hν higher than the bandgap of the material) is applied to the depletion region, electron hole pairs are generated. The carriers are swept away by an electric field; electrons moving towards n+ contacts, and holes moving to p+ contacts. Transport of the carriers induces an output current, I_{out}, at the terminals of the device.

The number of electrons generated per incident photon is defined as the quantum efficiency [33]:

$$\eta = \frac{I_p / q}{P_{opt} / h\nu} \tag{2.1}$$

where, I_p is the current generated by absorption of incident photons, P_{opt} is the optical power at a wavelength of λ (corresponding to a photon energy of hν).

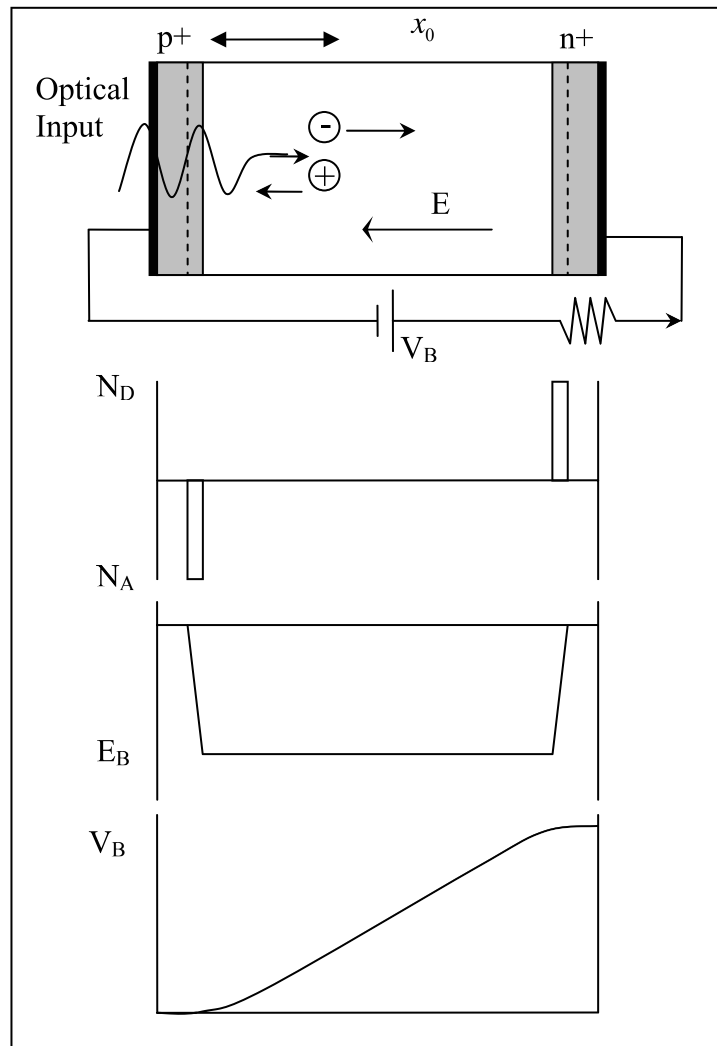

Figure 2.2: Distribution of dopant-ion charges, electric field and voltage for a p-i-n photodiode under reverse bias.

Another figure of merit is the responsivity, $\Re$, which is the ratio of the photogenerated current to the optical power:

$$\Re = \frac{I_p}{P_{opt}} = \frac{\eta q}{h\nu} = \frac{\eta\lambda(\mu m)}{1.24} \qquad (A/W) \tag{2.2}$$

Assume that, at $t = 0$, a narrow optical pulse generates carriers with a total charge of q, at a distance x_0, from p+ contact. Due to the electric field in the depletion region, positive and negative sheets of charges, with a surface charge density of $\sigma = q/A$, are forced to move in opposite directions, with velocities v_h and v_e, respectively. Each sheet contributes to the electric field formed between sheets:

$$E_\sigma = \frac{\sigma}{\varepsilon} = \frac{q}{A\varepsilon} \tag{2.3}$$

where ε is dielectric constant of the semiconductor. Direction of this extra electric field is opposite to the depletion region electric field, which results in a voltage drop across the depletion layer, as the sheets move away from each other [35].

This voltage drop can be expressed as:

$$V_\sigma(t) = \int_{x_h(t)}^{x_e(t)} E_\sigma dx = E_\sigma[x_e(t) - x_h(t)] \tag{2.4}$$

where $x_e(t)$ and $x_h(t)$ are the time dependent coordinates of the sheets. These coordinates can be expressed as:

$$x_e(t) = x_0 + v_e t \qquad 0 < t < t_e \tag{2.5}$$

$$x_h(t) = x_0 - v_h t \qquad 0 < t < t_h \tag{2.6}$$

where $t_e = (d - x_0)/v_e$ and $t_h = x_0 / v_h$ are electron and hole transit time. Assuming $t_e > t_h$, we can write time dependent voltage drop as:

$$V_\sigma = \begin{cases} \frac{\sigma}{\varepsilon}(v_e + v_h)t & ,0 < t < t_h \\ \frac{\sigma}{\varepsilon} v_e t & ,t_h < t < t_e \end{cases} \tag{2.7}$$

We can write the output current $I_{out}(t)$ as:

$$I_{out}(t) = \frac{dQ(t)}{dt} = \frac{d}{dt}\left[CV(t)\right] \tag{2.8}$$

Here, $C = \varepsilon A/d$, which is independent of bias voltage for p-i-n diode, and $V(t) = V_0 - V_\sigma(t)$, then time dependent current is:

$$I_{out}(t) = \begin{cases} I_1 = \frac{q}{d}(v_e + v_h) & ,0 < t < t_h \\ I_2 = \frac{q}{d} v_e & ,t_h < t < t_e \end{cases} \tag{2.9}$$

This expression is plotted in Fig. 2.3.

2.1.2 Detector Performance

The performances of photodetectors that are investigated in this work are efficiency and speed. Quantum efficiency of a detector, in which light partly transmits from the front surface and passes through the active layer once, is expressed as:

$$\eta = (1 - R)(1 - e^{-\alpha d}) \tag{2.10}$$

where R is the reflectivity of the front surface, α is the absorption coefficient, and d is the thickness that light travels in the region which absorbs. Using this equation, the efficiency can be maximized by minimizing the surface reflection,

increasing layer thickness, and playing with material to change absorption coefficient, or the effective absorption coefficient.

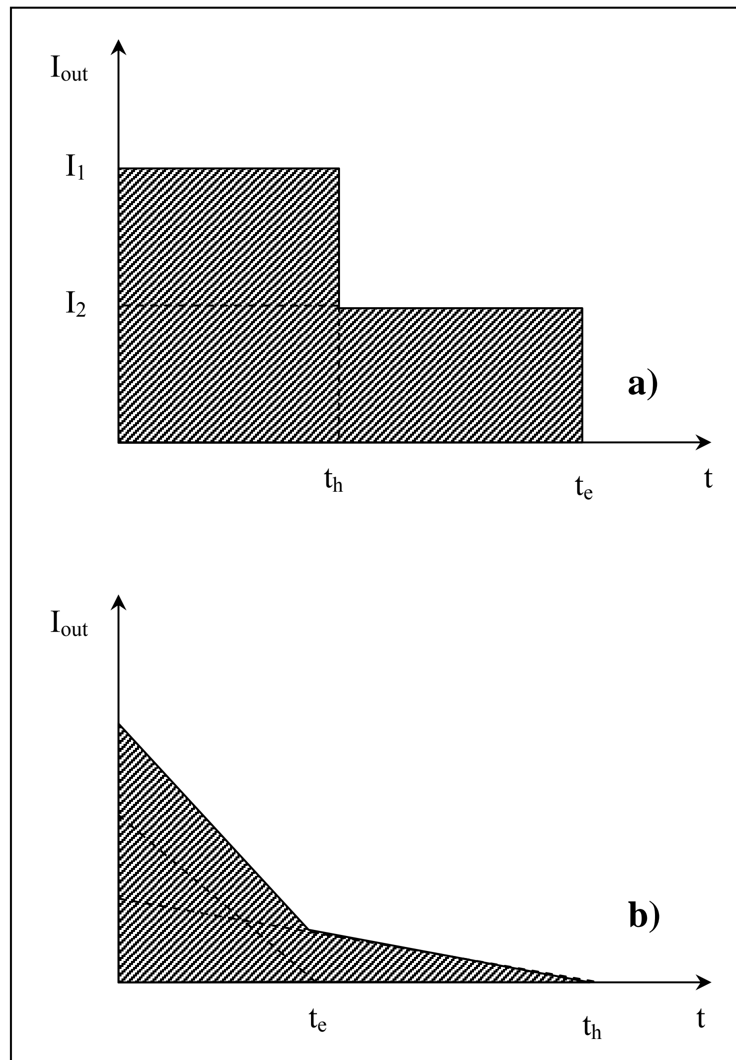

Figure 2.3: a) The induced current as a function of time, where photogeneration took place only at the sheet in the active region. b) Output current for uniformly illuminated diode, where electron drift velocity is larger than the hole drift velocity.

Another figure of merit is the bandwidth, or equivalently speed, of the diodes. The factors that limit the speed are the transit time of the carriers and RC time constant of the photodiode, which results from the intrinsic nature of the material and structure of the device.

For transit time limited case, the 3 dB roll-off frequency can be expressed as:

$$f_{tr} = 0.45\frac{v_e}{d} \tag{2.11}$$

For the RC constant limited case, same frequency is expressed as:

$$f_{RC} = \frac{1}{2\pi R_L C_d} \tag{2.12}$$

Photodiodes can be electrically modeled as in Fig. 2.4.

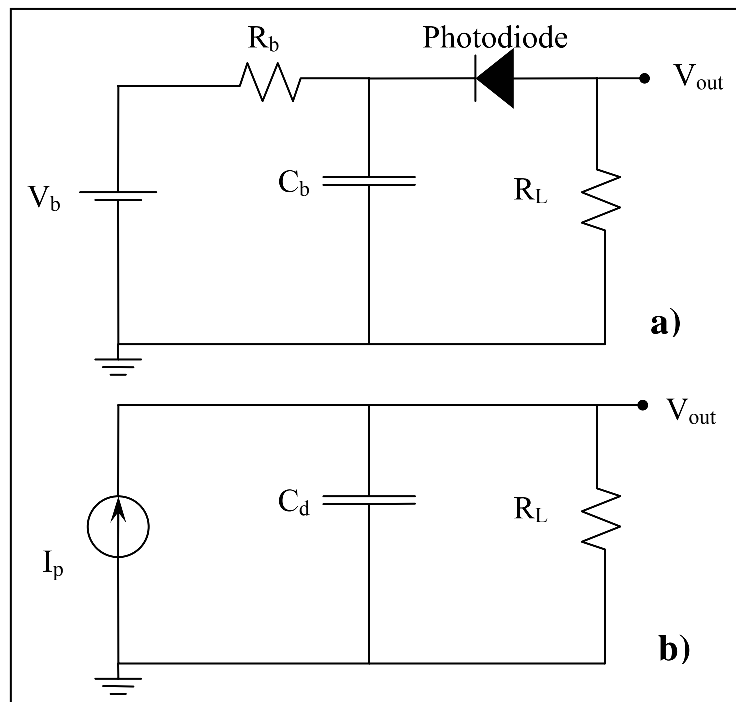

Figure 2.4: Schematics of photodiode circuitry under reverse bias (a) and equivalent high-speed model for frequency analysis (b).

2.2 Optical Multilayer Films

RCE device structures consist of tens of layers. So, they are difficult and expensive to grow. Also, optical properties of materials are wavelength dependent. All of this makes it necessary to use a good simulation method for analysis before ordering the structure for MBE growth. We used transfer matrix method (TMM), which provides a simple technique to calculate the electric field inside the structure.

However, this method requires some assumptions, and idealizes the structure. Interfaces are assumed to be completely flat, which is not always the case in semiconductor growth techniques. Materials are assumed to be defect free, so that extra scatterings within the structure are omitted.

We can think of successive layers as a repetition of two basic building blocks, with changing parameters. The first one is an interface of two different mediums, (Fig. 2.5), and the second is a homogeneous slab of one material, (Fig. 2.6). The simulation method simply combines these two and repeats the procedure for each successive layer.

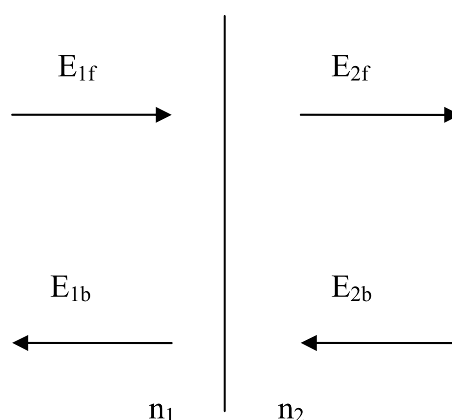

Figure 2.5: First building block of optical multilayer films; electric field is transferred from one side of a boundary to the other side.

Using continuity of electric and magnetic fields, electric fields at the left and right of any interface can be expressed as follows:

$$\begin{pmatrix} E_{1f} \\ E_{1b} \end{pmatrix} = \frac{1}{t_1} \begin{pmatrix} 1 & r_1 \\ r_1 & 1 \end{pmatrix} \begin{pmatrix} E_{2f} \\ E_{2b} \end{pmatrix} \tag{2.13}$$

where; $r_1 = (n_1 - n_2)/(n_1 + n_2)$ and $t_1 = 2n_1/(n_1 + n_2)$. Refractive index is defined as the square root of the dielectric constant; $n = \sqrt{\varepsilon - j\varepsilon'}$, where the imaginary part is due to absorption in the medium. Using the above equality, we have transferred fields at the left of the interface to the right.

The electric field that traveled in the second medium can be found using the propagation of a plane wave.

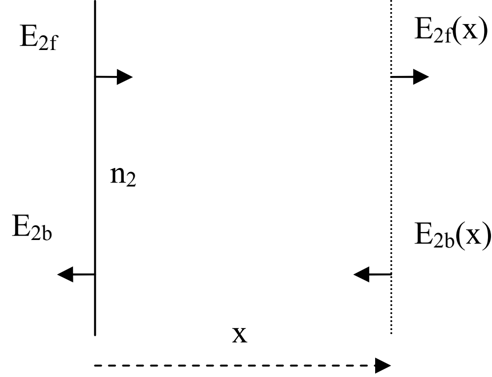

Figure 2.6: Second building block of optical multilayer films: Electric field is transferred, or propagated, inside a homogeneous medium.

$$\begin{pmatrix} E_{2f} \\ E_{2b} \end{pmatrix} = \begin{pmatrix} e^{jkx} & 0 \\ 0 & e^{-jkx} \end{pmatrix} \begin{pmatrix} E_{2f}(x) \\ E_{2b}(x) \end{pmatrix} \tag{2.14}$$

where $k = 2\pi n/\lambda$. Combining these two building blocks, we can evaluate the transfer matrix of electric fields from the start of a layer interface to the next layer's interface as follows:

$$\mathbf{T}_i = \frac{1}{t_i}\begin{pmatrix} e^{j\delta_i} & r_i e^{j\delta_i} \\ r_i e^{-j\delta_i} & e^{-j\delta_i} \end{pmatrix} \tag{2.15}$$

where $r_i = (n_i - n_{i+1})/(n_i + n_{i+1})$, $t_i = 2n_i/(n_i + n_{i+1})$, and $\delta_i = k_i d_i$. Cascading these matrices for N layers, the total transfer matrix for the multilayer system becomes:

$$\mathbf{T}_{\text{total}} = \mathbf{T}_0\mathbf{T}_1 \cdots \mathbf{T}_{\text{N-1}}\mathbf{T}_{\text{N}} \tag{2.16}$$

Electric field before and after any stack of arbitrary layer combination becomes;

$$\begin{pmatrix} E_{\text{bf}} \\ E_{\text{bb}} \end{pmatrix} = \mathbf{T}_{\text{total}} \times \begin{pmatrix} E_{\text{af}} \\ E_{\text{ab}} \end{pmatrix} \tag{2.17}$$

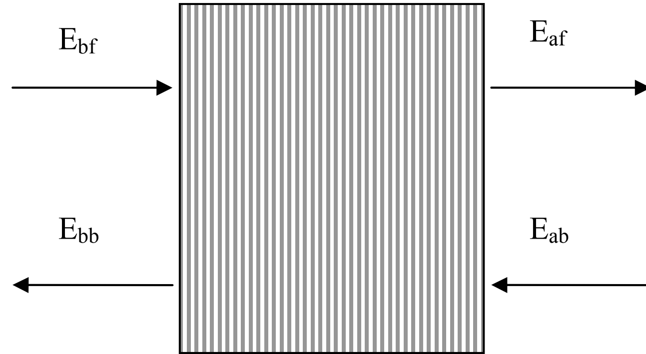

Figure 2.7: A general multilayer film, with electric fields before and after the stack.

We need to find the reflected power, since measurement devices detect power and not the electric field. Power can be found using:

$$\vec{S} = \vec{E} \times \vec{H} \tag{2.18}$$

For a plane wave:

$$\vec{H} = \frac{1}{\omega\mu}\vec{k} \times \vec{E} \tag{2.19}$$

From these equations, it is apparent that power is proportional to the square of the electric field and the refractive index of the medium. Reflectivity and transmittivity can be found using:

$$R = \frac{|E_{\mathrm{bb}}|^2}{|E_{\mathrm{bf}}|^2} \tag{2.20}$$

$$T = \frac{|E_{\mathrm{af}}|^2 n_{\mathrm{final}}}{|E_{\mathrm{bf}}|^2 n_{\mathrm{incident}}} \tag{2.21}$$

Absorption in any medium, which we use when simulating quantum efficiency, can be found using power going inside the medium and power getting out of the medium.

2.3 Resonant Cavity Enhancement

In optical communication and measurement systems, detectors with high efficiencies and high bandwidths are required to compensate system losses and to carry maximum information, respectively. In an ordinary semiconductor photodetector, efficiency depends on the thickness of the region where light is absorbed. For example, with an absorption coefficient of $\alpha : 10^4 cm^{-1}$, typical for GaAs, to collect 80% of all incoming light, excluding reflection losses, it is required about $1.6\mu m$ long active region. On the other hand, bandwidth of this device is severely limited by this thickness, since carriers have to pass through the entire device. Therefore, (bandwidth)$\times$(efficiency) product (BWEP) is a figure of merit for high-speed photodetectors.

To increase BWEP requires special techniques because it depends on the physics of the device and material properties. Enhancement of the electric field inside the active region was one solution to this trade off. In this method, the active region is placed between two mirrors, so that light travels the same

region several times, being partially absorbed more than once. Detectors with this kind of structure are called resonant cavity enhanced (RCE) photodetectors.

Resonant cavity enhancement of an electric field inside the device can be considered completely analogous to the enhancement of resonance currents in a series RLC circuit. As current can be much larger than the current source in the circuit, electric field in the cavity can also be larger than the incoming electric field, which increases the efficiency.

2.3.1 Formulation

Figure 2.8 shows a generalized structure of an RCE photodetector. Since our purpose is to achieve the maximum absorption efficiency, distributed bragg reflector (DBR) mirrors are assumed to be lossless, i.e. the materials for mirrors do not absorb around the wavelength of interest. Also, the normal incidence of a plane wave to the front surface of the device is assumed in the following formulation. In an oblique incidence case, i.e. angle dependence of device properties can easily be found by properly exchanging thickness, reflection and transmission coefficients in the procedures [24]. Plane wave approach is enough for our purposes.

The active layer, with a thickness of d and an absorption coefficient of α, is placed between two DBR mirrors. In the figure, L_1, L_2 and L are the distances between the front mirror and active region, active region and back mirror, and front mirror and back mirror respectively. Field reflection coefficients from mirrors are $r_1 e^{-j\phi_1}$ and $r_2 e^{-j\phi_2}$, where ϕ_1 and ϕ_2 are phase shifts due to collective reflection mechanism in DBRs. Absorption coefficient outside the active region is α_{ex}. E_i, E_f and E_b are the electric field amplitude

of incident light, forward traveling field amplitude at $z = 0$ and backward traveling field amplitude at $z = L$ respectively.

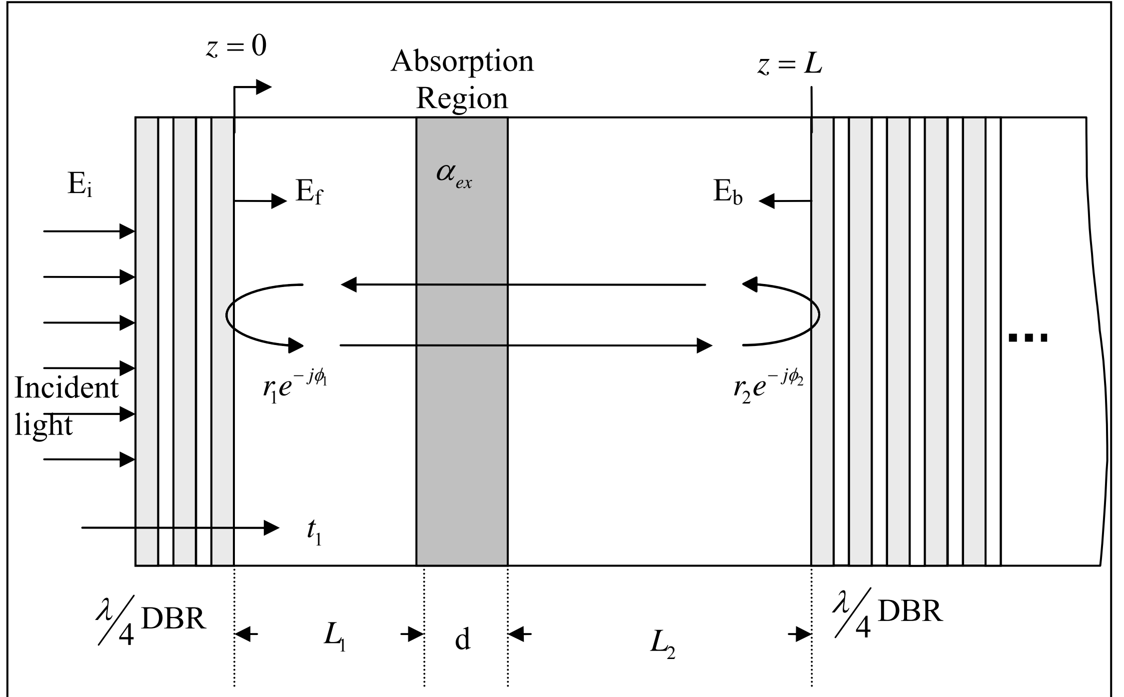

Figure 2.8: Lateral structure of RCE photodetector

E_f consists of a transmitted field through the front mirror and reflected backward traveling field from the front mirror. Therefore, E_f at $z = 0$ can be written as:

$$E_f = t_1 E_i + r_1 r_2 e^{-\alpha d - \alpha_{ex}(L_1 + L_2)} e^{\cdot} \tag{2.22}$$

where $k = 2\pi n/\lambda_0$, where n is refractive index of cavity material of interest.

Solving for E_f gives:

$$E_\mathrm{f} = \frac{t_1}{1 - r_1 r_2 e^{-\alpha d - \alpha_{ex}(L_1+L_2)} e^{j(2kL+\phi_1+\phi_2)}} E_\mathrm{i} \tag{2.23}$$

and backward traveling wave at $z = L$ becomes:

$$E_\mathrm{b} = r_2 e^{-\frac{\alpha d}{2}} e^{-\frac{\alpha_{ex}}{2}(L_1+L_2)} e^{-j(kL+\phi_2)} E_\mathrm{f}\,. \tag{2.24}$$

The optical power inside the cavity is given by:

$$P = \frac{n}{2\eta_0}|E|^2 \tag{2.25}$$

where η_0 is the vacuum characteristic impedance of electromagnetic waves, and $E = E_\mathrm{f} + E_\mathrm{b}$ at any point in the cavity.

The light power absorbed inside the active layer, P_l, can be obtained from the incident power, P_i, as:

$$\begin{aligned} P_l &= (P_f e^{-\alpha_{ex}L_1} + P_b e^{-\alpha_{ex}L_2})(1 - e^{-\alpha d}) \\ &= \frac{(1-r_1^2)(e^{-\alpha_{ex}L_1} + r_2^2 e^{-\alpha_{ex}L_2} e^{-\alpha_c L})(1 - e^{-\alpha d})}{1 - 2 r_1 r_2 e^{-\alpha_c L}\cos(2kL + \phi_1 + \phi_2) + (r_1 r_2)^2 e^{-2\alpha_c L}} \times P_i \end{aligned} \tag{2.26}$$

In this equation, standing wave effect is neglected for now, and $\alpha_c = (\alpha_{ex}L_1 + \alpha_{ex}L_2 + \alpha d)/L$. Assuming all carriers generated by absorption contributes to the detector current, η is the ratio of the absorbed power to the incident optical power, $\eta = P_l/P_i$. Therefore:

$$\eta = \left\{ \frac{(e^{-\alpha_{ex}L_1} + R_2 e^{-\alpha_{ex}L_2} e^{-\alpha_c L})}{1 - 2\sqrt{R_1 R_2} e^{-\alpha_c L}\cos(2kL + \phi_1 + \phi_2) + R_1 R_2 e^{-2\alpha_c L}} \right\} \times (1 - R_1)(1 - e^{-\alpha d}) \tag{2.27}$$

.

In a practical detector design $\alpha_{ex} << \alpha$, so α_{ex} can be neglected and the terms inside the curly braces, which is called the enhancement, can be rewritten as:

$$enhancement = \frac{(1+R_2 e^{-\alpha d})}{1-2\sqrt{R_1 R_2}e^{-\alpha d}\cos(2kL+\phi_1+\phi_2)+R_1 R_2 e^{-2\alpha d}}. \quad (2.28)$$

2.3.2 Standing Wave Effect

In the above derivations, the spatial distribution of power inside the cavity and active region was neglected. This distribution arises from the standing wave formed by two counter-propagating waves. Therefore, η is a function of placement of active region. This effect is called the standing wave effect (SWE). When an active region spans several wavelengths, this effect is not very important, but for thin active layers, SWE must be considered.

SWE can be included in the formulation simply as an effective absorption coefficient, so that $\alpha_{eff} = SWE \times \alpha$, which is either increased or decreased by the placement of active layer and active layer thickness. Effective absorption coefficient can be expressed as:

$$\alpha_{eff} = \frac{1/d\int_0^d \alpha(z)|E|^2(z,\lambda)dz}{2/\lambda\int_0^{\lambda/2}|E|^2(z,\lambda)dz} \quad (2.29)$$

where $\lambda = \lambda_0/n$, $E(z,\lambda)$ is the total electric field in the cavity at a given wavelength, and the denominator is the average of the electric field.

2.4 Design of the Photodetector

In the previous sections, we have reviewed the basic tools for designing the diode, i.e diode characteristics; the basic simulation tool used in reflectivity, absorption and layer structure; RCE effect that constitutes the building block of our design. For a good design, being aware of the material properties and creating the design accordingly is crucial. Low-loss cavity is very important for limiting absorption to the active layer only. High reflectance bottom mirror, which is designed with non-absorbing materials, increases both the quantum efficiency and quality factor of the cavity.

So, we first need to review the properties of LT-GaAs, which is described in the next section.

2.4.1 LT-GaAs Material Properties

LT-GaAs was discovered at Lincoln Laboratory in the mid 1980s and has been applied to electronic and photoconductive devices and circuits ever since [36]. At first the main use was for eliminating the effects of back- and sidegating in GaAs circuits [7]. Most importantly for device applications, the large excess As concentration in LT-GaAs results in a large trap density, that in turn results in a high resistivity, a large breakdown field, and an extremely short photoexcited carrier lifetime. Properties of MBE grown GaAs vs. LT-GaAs are shown in Table 2.1 [36, 37].

Buried Schottky barrier model is generally used to explain the effect of excess As content on GaAs material. According to this model, the As precipitates (principally hexagonal As and a semimetal) form a Schottky barrier with respect to the matrix, depleting a portion of the surrounding space.

If the doping density is high, or if the precipitates are sufficiently widely spread, depletion regions do not overlap, producing a material with relatively high conductivity. For less heavily doped material, or for more closely spaced precipitates, the overlapping depletion zones pinches off the conducting paths, producing a material with very high resistivity [37].

	MBE GaAs	**LT-GaAs**
Growth Temperature	600 ºC	~200 ºC
Structure	Crystalline	Crystalline
Stoichiometry	50 : 50	~1% excess As
Resistivity	~0.3 - 20 Ω-cm	~10^6 Ω-cm
Breakdown Field	~3 x 10^4 V/cm	~5x10^5 V/cm
Trap Density	< 10^{15} cm-3	~ 10^{19} cm-3
Lifetime for excited charges	~1 ns	~150 fs
Overgrowth	Excellent	Excellent

Table 2.1: Comparison of the properties of LT-GaAs with undoped GaAs grown by MBE.

Metallic As precipitates exhibit characteristic barriers heights around 0.7 eV (corresponding to 1.7 μm). Thus, photons with wavelengths up to 1.7 μm can be absorbed by LT-GaAs, where the cut-off wavelength of GaAs was at 0.87 μm.

Despite the excellent properties listed in Table 2.1, there is a drawback of LT-GaAs, namely its low absorption coefficient. In the previously fabricated detectors, quantum efficiencies around and smaller than 1% at 1310 and 1550

nm with vertically illuminated p-i-n, traveling-wave p-i-n and metal-semiconductor-metal photodetectors have been reported [7, 12, 13, 17, 38, 39] all of which suffer from low efficiencies.

	Refractive Index	1/e Absorption Length
GaAs at 850 nm	3.66 - j 0.063	2.15 μm
LT-GaAs at 1310 nm	3.41 - j 0.012	17.37 μm
LT-GaAs at 1550 nm	3.37 - j 0.0045	54.82 μm

Table 2.2: Absorption lengths of GaAs and LT-GaAs at different wavelengths, where detectors were fabricated [3].

2.4.2 Cavity Design

For a good performance, cavity parameters of a detector must be chosen suitably. The placement of an active region inside the cavity, top and bottom mirror reflectivities and materials for mirrors are the variables that should be optimized. RCE structures require a bottom mirror with high reflectivity. Reflectance of metals at optical and infrared wavelengths is less than 95%. Instead, Distributed Bragg Reflectors (DBR) are widely used in optoelectronic applications, such as in lasers, detectors, photonic crystals; integrated with the devices or separate components in setups, or even the device itself. A DBR consists of periodic layers of two or more materials. If it is used for a certain wavelength interval, such as our application around 1550 nm, two materials of contrasting refractive indexes are enough to achieve almost 100% reflectivity. This can be achieved using a moderate number of pairs, depending on the contrast ratio of the refractive indexes. Each pair consists of two layers with refractive indices n_1 and n_2 with layer thickness of $\lambda_c / 4n_1$ and $\lambda_c / 4n_2$

respectively, where λ_c is the central wavelength for the mirror. Using simple transmission line analysis, maximum reflectivity of DBR can be expressed as:

$$R_{\max} = \left| \frac{\left(\frac{n_2}{n_1}\right)^{2N} n_0 - n_s}{\left(\frac{n_2}{n_1}\right)^{2N} n_0 + n_s} \right|^2 \tag{2.30}$$

where N is the number of layer pairs, n_0 is refractive index of the medium before DBR, n_s is refractive index of the medium after DBR, i.e. of the substrate. As the DBR materials at 1550 nm, we chose GaAs (n = 3.41) and AlAs (n = 2.88), with a thickness of 134.3 and 113.6 nm respectively, that gives more than 99% reflectivity with mediums around GaAs. The length of LT-GaAs is chosen as one wavelength, for both absorbing more optical power and to balance any growth rate fluctuations. We placed an extra n- layer beneath active region to make electron and hole effective drift times closer to each other, for high-speed considerations.

In Fig. 2.10 and 2.11, we simulated reflectivity, transmittivity and absorption in the active region.

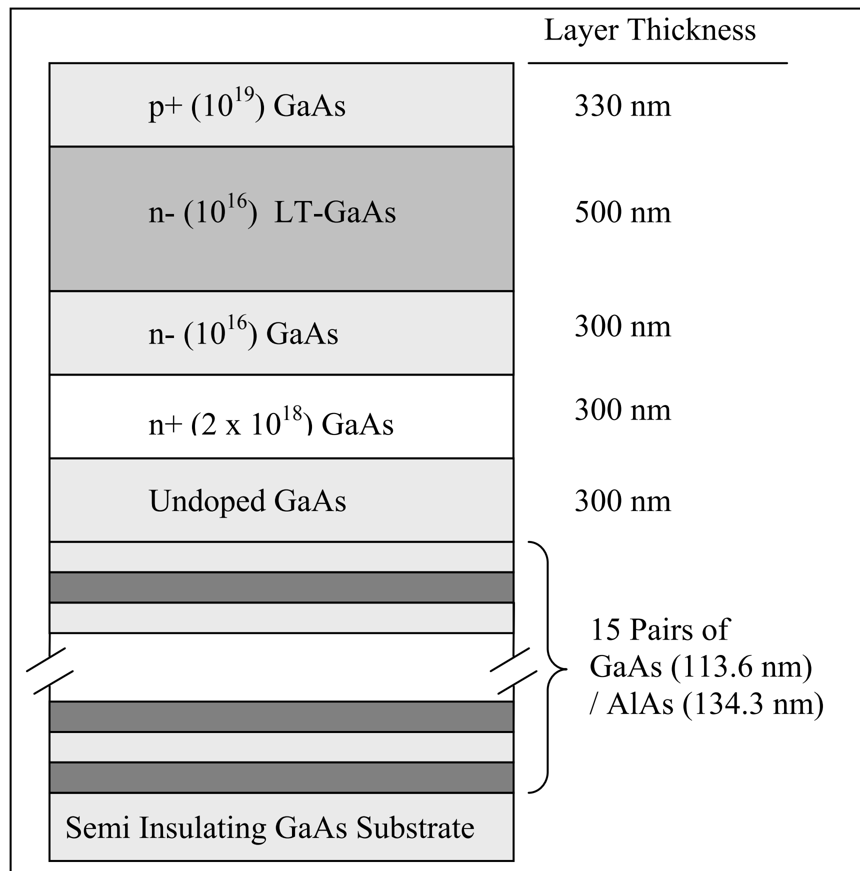

Figure 2.9: Epitaxial structure of LT-GaAs wafer

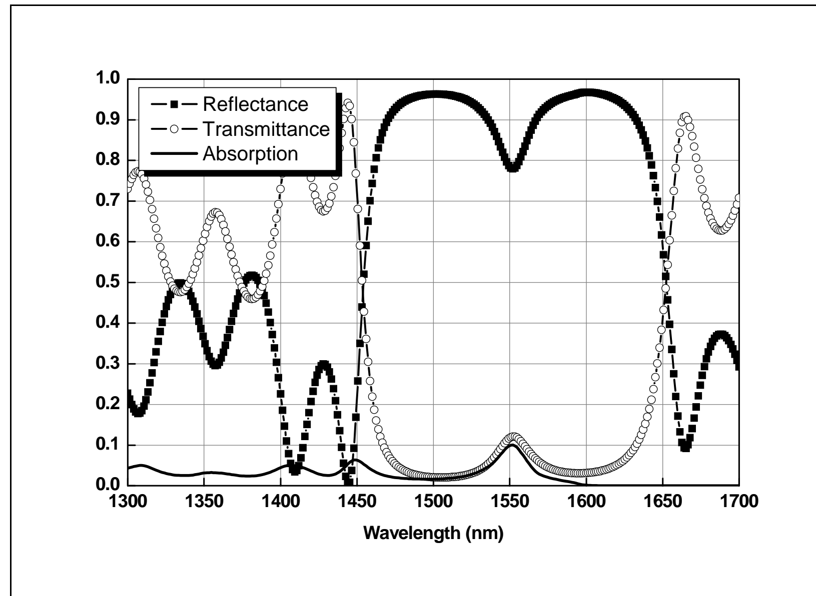

Figure 2.10: Simulated absorption at the active region, reflectance and transmittance of the LT-GaAs wafer.

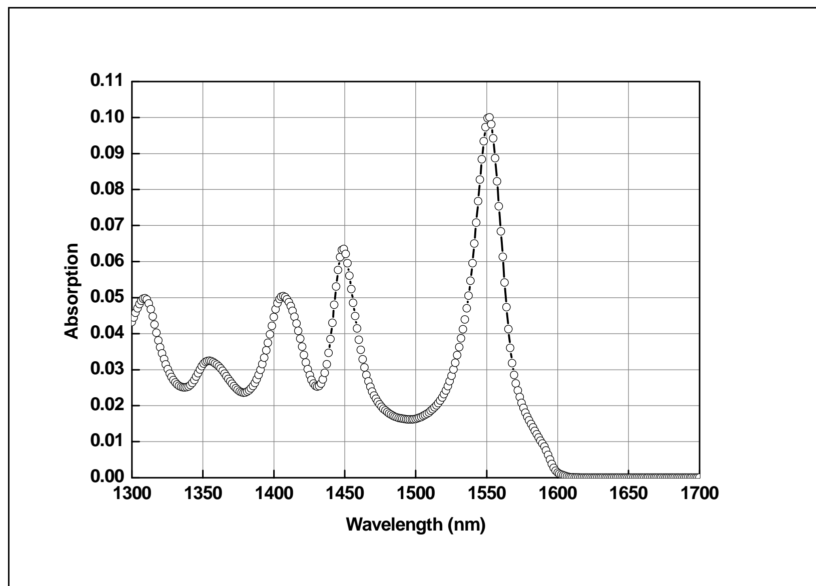

Figure 2.11: Simulated absorption at the active region.

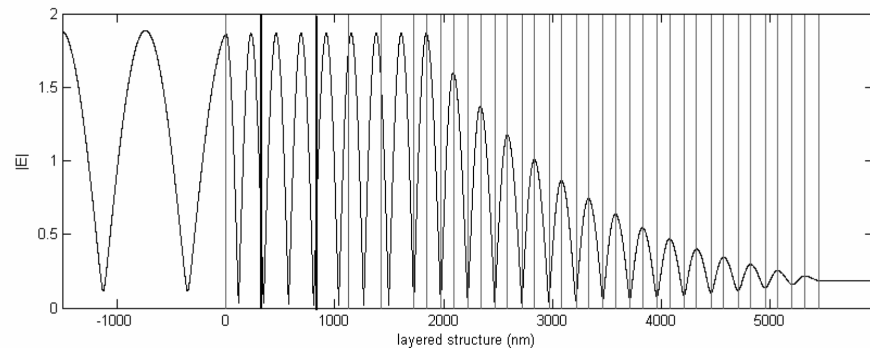

Figure 2.12: Electric field distribution throughout the epitaxial structure. The point ‘0 nm’ is the front surface of the wafer, and the area between the bold lines is the active area.

Chapter 3

Fabrication

The fabrication of photodetectors requires several steps in succession and each of these contribute to the optical and electrical response of the devices. These include steps such as ohmic contact deposition, air bridge formation, and top DBR deposition. The process steps for our detectors are the same as the normal GaAs process that was developed by the previous graduate students. Although DBR deposition is very important for efficiency in RCE detectors, we did not perform it in the LT-GaAs process.

All of the fabrication processes are completed in Class-100 Clean Room of Advanced Research Laboratory.

3.1 Molecular Beam Epitaxy

Vapor phase epitaxy (VPE) and in particular metal-organic chemical vapor deposition (MOCVD) and molecular beam epitaxy (MBE) are major growth techniques of GaAs [40]. In MOCVD growth, the Ga, As, and dopant atoms are brought to the wafer in the gaseous phase and is linked to other molecules. Under appropriate temperatures, reactions take place on the surface of the substrate that result in these atoms being deposited on the surface, where they replicate the underlying crystal structure. Since MOCVD requires certain high temperatures, where Ga and As are not in solid form, it is impossible to grow

LT-GaAs as a part of the epitaxial structure by way of this method. MBE has significant advantages over MOCVD, but is more expensive. In this procedure, the substrate is placed in a high vacuum and elemental species are evaporated from ovens, Fig. 3.1, and impinge upon the heated substrate, here they assemble into crystalline order. With proper control of the sources and temperature, almost any material composition and doping can be achieved. Further, the composition may be controlled with a resolution of virtually one atomic layer. For temperature consideration, LT-GaAs wafers are grown in MBE machines.

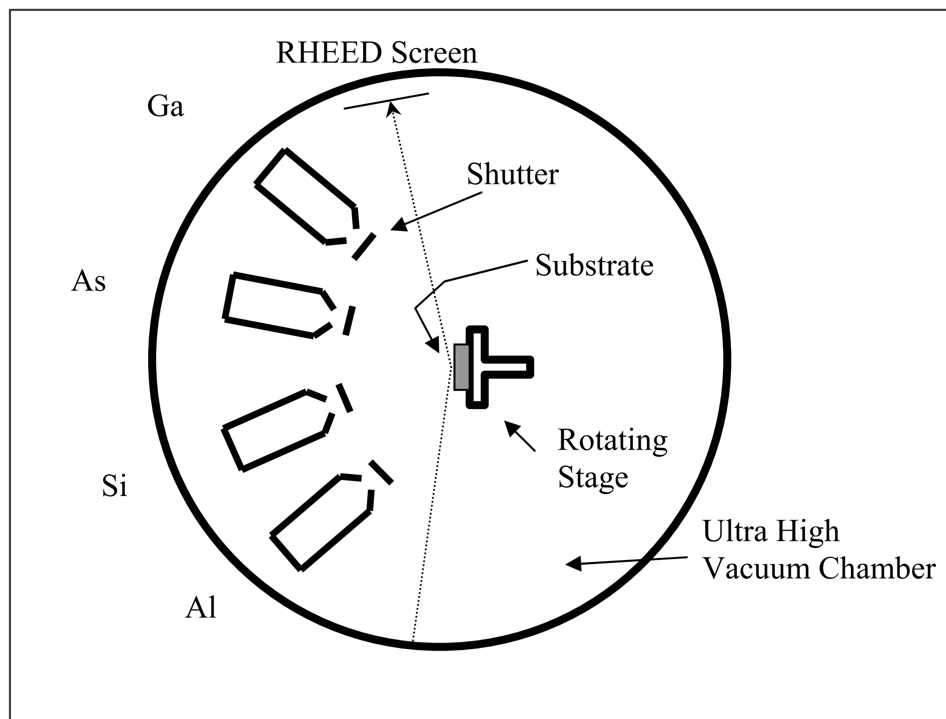

Figure 3.1: Schematic diagram of MBE system.

Wafers were grown in two different MBE machines in USA and Spain. USA wafers were of two kinds; one was with bottom DBR, i.e. RCE structure, and one without, i.e. single pass. Spain wafers were only RCE structured wafers.

Samples were grown on 3-inch semi-insulating GaAs wafers (100). After thermal oxide desorption, a 0.15 μm GaAs buffer layer was grown before the bottom GaAs/AlAs Bragg reflector. The reflector consisted of 15 pairs of undoped GaAs (113.6 nm) and AlAs (134.3 nm) layers grown with a substrate temperature T_s = 600 °C. On top of the reflector an undoped GaAs layer (300 nm) was grown at T_s = 550 °C and two n-type GaAs:Si layers with $n^+ = 2\times10^{18}$ cm^{-3} (300 nm) and $n^- = 1\times10^{16}$ cm^{-3} (300 nm) were grown at the same substrate temperature. As_4 flux was kept at 1×10^{-5} mbar during all of the growth (As_4/Ga flux ratio around 25). Reflection high-energy electron diffraction (RHEED) pattern was streaky along the growth of the mirror. The substrate temperature was decreased to 200 °C for the 500 nm thick lightly doped LT section of the detector ($n^- = 1\times10^{16}$ cm^{-3}). During this stage the RHEED showed a slightly hazy pattern and a decrease in the diffracted intensity with time, but still showing long lines. This RHEED pattern is attributed to an increment of the surface roughness due to the As in excess that is present on the surface. After this layer the substrate temperature was increased again to T_s = 550 °C and a streaky and clearly defined RHEED (2×4) pattern was recovered during the growth of the top p-type GaAs:Be layer ($p^+ = 1\times10^{19}$, 330 nm). To compare the performance of the RCE photodiode samples with conventional single-pass photodiodes, a non-resonant detector wafer was also grown with the same growth parameters except for the bottom Bragg mirror [41]. In Fig. 3.2, epitaxial structure of Spain wafer is shown, both in normal mode and

compositional mode, where a fingerprint of growth discontinuity is clearly seen in the second pair of DBR.

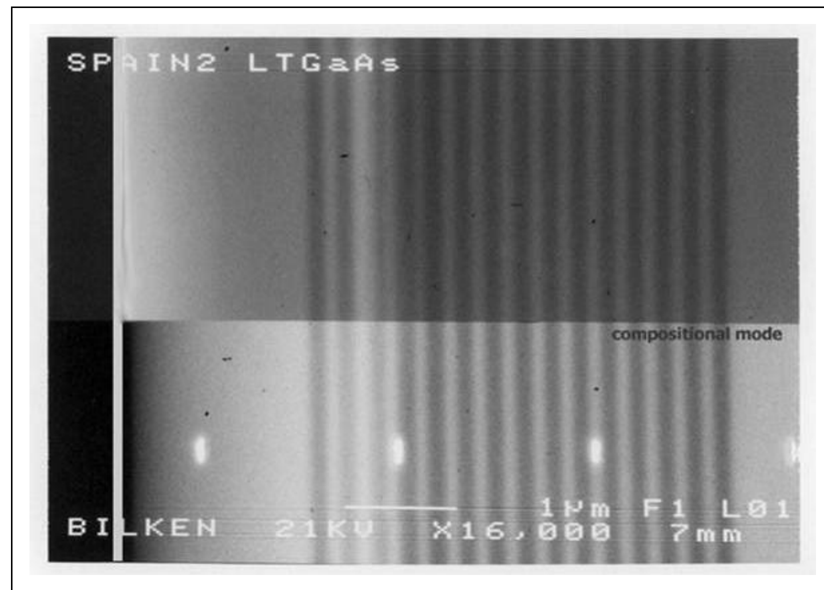

Figure 3.2: Scanning electron microscope image of the wafer.

3.2 Basic Process Steps

3.2.1 Wafer Cleaving and Sample Cleaning

Wafers are cleaved into smaller pieces, because growth is very expensive and by this several different processes using the same wafer is possible. Wafers, with surfaces having crystal direction (100), had two flats and the cleaving directions were perpendicular to these. A diamond tipped scribing tool is used to lightly scratch a starting point at the edge of wafer. Then, a small pressure is enough to divide the wafer. Wafer cleaving of GaAs is easier and more regular

than other semiconductors, such as Si and GaN. Samples were about 8 mm x 8 mm and masks were about 6 mm x 6 mm.

Cleanliness is crucial to achieve a high yield on one sample and to reproduce the process in the following runs [40]. After cleaving, yet before fabrication and between all of the steps, a chemical cleaning is applied to ensure the best performance. This keeps away the particles of environmental and chemical contaminations from the preceding process steps.

Chemical cleaning consists of dipping the sample into three solvents, rinsing with water and subsequently drying. First, samples were immersed into trichloroethane (TCE) at room temperature and boiled for 2 minutes on hot bake. Second, the samples are kept in acetone for 5 minutes. Third, they are immersed into isopropanol and boiled for 2 minutes. In this sequence, TCE dissolves oil; acetone dissolves TCE, organic molecules, photoresist residues and isopropanol dissolves acetone. Then, samples are rinsed in the deionized (DI) water flow and dried with a nitrogen gun. The cleaning step ends with the dehydration bake at 120 °C for 2 minutes.

3.2.2 Photolithography

Photolithography is the process of transferring patterns on a photomask onto a thin layer of radiation sensitive material (photoresist), which covers the surface of semiconductor or a coating on semiconductor. Patterns on the photomask define the regions to be etched, or coated, such as ohmic contacts, mesa isolations, capacitors and interconnect pads. Then, etching or coating is performed and resist is cleaned afterwards.

In our process, we used AZ5214E type photoresist, which is a positive photoresist and meets the requirements of minimum feature size (~ 1 μm),

sensitivity (~360 nm, spectral absorption peak), adhesion, as well as etch resistance [34]. Karl Suss MJB3 Mask Aligner is used for alignment and exposure. AZ400K developer is used for etching away exposed areas of photoresist.

First, Hexametyldisilazane (HMDS) is coated on the samples as an adhesion promoter and spun at 5000 rpm for 20 sec. Then, photoresist is coated and spun at 5000 rpm for 40 sec. Resulting resist thickness is about 1.3 μm, obeying the empirical formula:

$$Resist\ thickness\ (\mu m) = 88.55 / \sqrt{spin\ speed\,(rpm)} \qquad (3.1)$$

Following the resist application, samples are soft-baked at 110 ºC for 50 sec. Samples are, then, exposed to 365 nm radiation from a Hg lamp through mask aligner. The exposure step differs for two PL methods:

Normal Photolithography: Samples are exposed to UV light for about 40 sec at 4mW/cm^2, making 160 mJ/ cm^2. This method is used for thin metallization, etch steps and the post step.

Image Reversal Photolithography: Samples are exposed to 60 mJ/ cm^2. Then, they are baked at 110 ºC for 2 min, and after that, exposed again to UV light for 60 mJ/ cm^2. This is used for thick metallization, in which we mostly have a liftoff problem.

Developer is prepared as 1:4 (AZ400K:H_2O) ratio. As the desired features are etching away, color change can be observed, and after the change is finished the samples are rinsed with DI water and dried using a nitrogen gun. Alignment and development are checked under an optical microscope. For a good process, resolution patterns must be sharp and ~1μm resolution is achieved if development patterns show a grating-like color change.

To make photoresist mushroom-like, so that no metal deposits to the sidewalls, samples sometimes remained in chlorobenzene for 10 min.

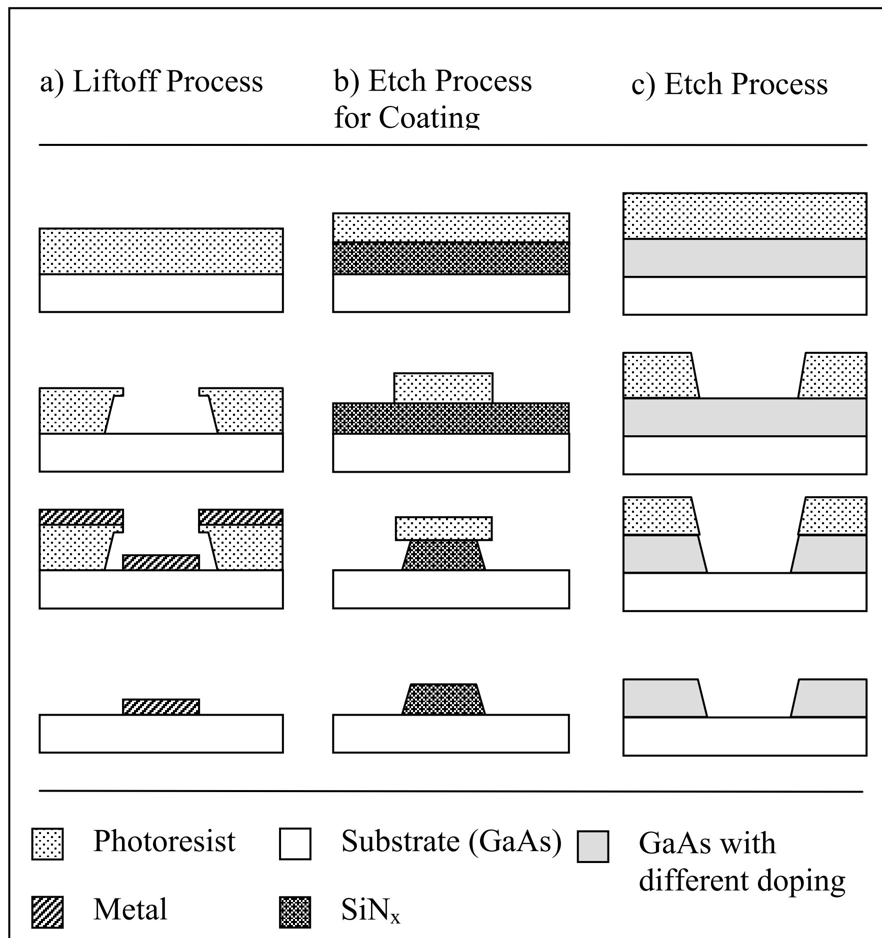

Figure 3.3: Basic resist processes: a) Liftoff process for all metallization steps, b) Etch process for coatings, only at SiN_x passivation coating step, c) Etch process for ohmic and mesa etch steps.

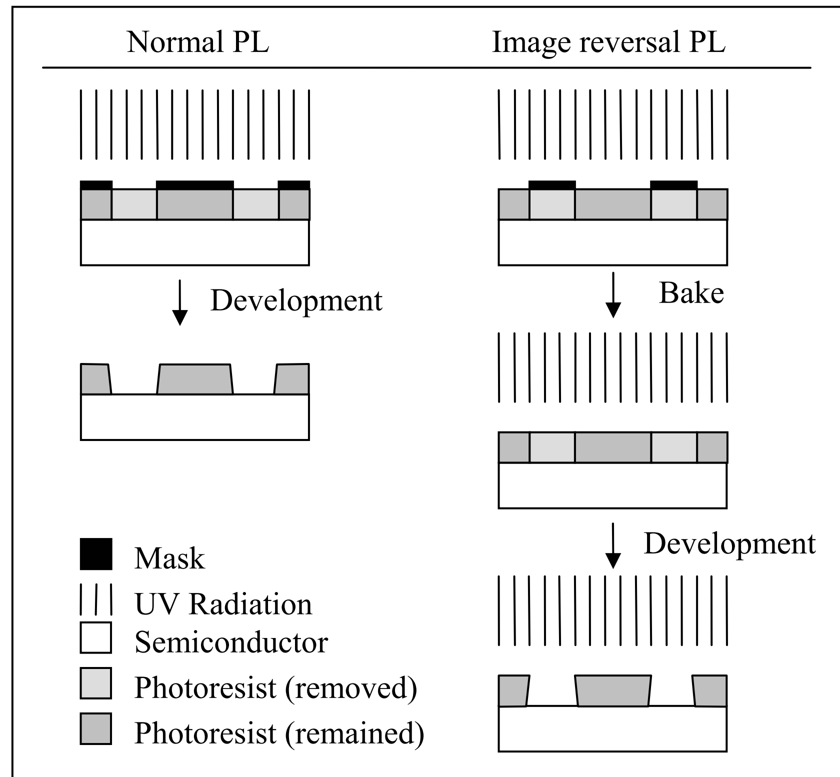

Figure 3.4: Normal PL, and Image Reversal PL. Note to the photoresist walls in either case. Image Reversal PL method makes the liftoff process easier.

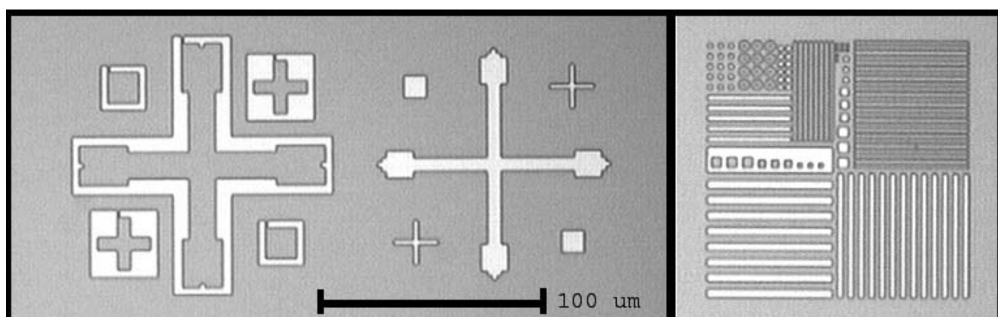

Figure 3.5: Alignment marks and the development pattern after the first PL, i.e. no alignment made yet. Gray areas are photoresist. Upper right quarter of the development patterns has 25 of 1 µm wide grooves separated by 1 µm.

3.2.3 Etching

Etching is used to transform the patterns defined by PL, to underlying layers, such as a semiconductor, metal or dielectric coatings, so that these layers are also patterned like the mask by means of PL. We also used etching to clean resist after the process steps, to thin resist for the post opening step and to remove oxides from surfaces. Two types of etching are used in the GaAs process:

Wet Etching: The main mechanism of wet etching is the chemical reactions at the surface of the substrate with etchants. We used NH_3:H_2O_2: H_2O solution to etch GaAs layers. Like many other etchants [3, 40], the etching mechanism first oxidizes the surface and then removes the oxides by acid or base. H_2O_2 is the agent responsible for oxidation and NH_3 is the agent base. With 8:2.4:300ml (25%NH_3:H_2O_2: H_2O) mixture, etch rate was about 50 Å/sec. Etching is isomorphic enough that there was not any problem in small dimensions. To etch SiN_x (nitride film), we used buffered HF (1:100); the etch rate was about 30 nm/sec. Before etch step, photoresist might be baked at 120 ºC for 1 min [3], if the etch thickness was more than photoresist thickness (~1.3 µm), since the etchant also etches resist. Wet etching is used at ohmic contact formations, mesa isolations of the devices, and patterning dielectric layer.

Dry Etching: There are several dry etching techniques being used in semiconductor fabrication processes, such as plasma etching, reactive ion etching, reactive ion beam etching and ion milling [40]. In the Advanced Research Laboratory, we use only Reactive Ion Etching (RIE), which uses directional ion bombardment and utilizes chemical etching. The most important property of RIE is its directionality, i.e. the vertical etch rate is much higher

than the lateral etch rate, so very reliable and isomorphic etching can be made with RIE. We use dry etching for thinning photoresist at a step that requires certain resist thickness throughout the sample, since using wet etching we cannot obtain this flatness. O_2 is used to etch resist, with given parameters shown in Table 3.2. After the top DBR coating process, SiN_x and SiO_2 could be etched using CCl_2F_2.

3.2.4 Thin Film Coating

Film coating is the third building block of the semiconductor process, along with PL and etching. Our process contains two different film coatings. The first one is a metal (Ti, Au, Ni, Ge) coating for ohmic contacts, interconnect pads, and air bridges. The second one is dielectric coating. It functions as a passivation layer of the device from the atmosphere, a dielectric material for metal-semiconductor-metal capacitors, anti-reflection or reflection layers.

Metals depositions were performed using a UHV LE590 box coater. Metals were placed into tungsten boats that also behave as resistances to be heated by electrical current for evaporation. Box was vacuumed and during the evaporation, deposited metal thickness was monitored with detectors. Therefore, the thickness of the deposited films can be controlled accurately.

Dielectric coatings (SiN_x, SiO_2) are deposited by plasma enhanced chemical vapor deposition (PECVD). Metals on the devices require relatively low temperatures after deposition and PECVD allows low temperature for dielectric depositions. Gases used for dielectrics are silane (2% SiH_4 + 98% N_2), ammonia (NH_3), and N_2O. For SiN_x, reactants are silane and ammonia; for SiO_2, silane and N_2O. Parameters are shown in Table 3.2.

3.3 Device Process Steps

Devices are fabricated using a microwave compatible process. There were two different mask sequences. In the first one, devices have relatively large sizes, up to 200 µm diameter, to collect all the incoming light for efficiency measurement. In the second mask sequence, devices have mostly small sizes, down to 5 µm x 5 µm square active area. Process steps for two masks differ after the thermal annealing step.

3.3.1 Cavity Tuning

Epitaxial structure is designed so that the resonance wavelength is at 1550 nm exactly. However, due to growth, layer thicknesses were deviated from the desired values. We first determined the wafer structure using reflectance measurement and TMM simulations that we developed, then shifted the absorption peak to 1550 nm by surface etch.

Reflection measurement is performed using an Ocean Optics reflection probe. This data provides unique information about layer thicknesses. According to this data, we etched the surface of the sample by 25%NH_3:H_2O_2: H_2O (8:2.4:600) etchant iteratively, by an etch rate of ~25Å/sec. So, devices are tuned to 1550 nm within ~ ±2 nm, before following the fabrication steps, as it is seen in Fig. 3.6.

3.3.2 Ohmic Contact Deposition and Thermal Annealing

After ohmic contact PL, samples are etched down to the middle of n+ layer (~1300 nm) in several steps. The etch depth is measured with a DekTak profilometer at each step. Then, n+ metallization is performed as shown in

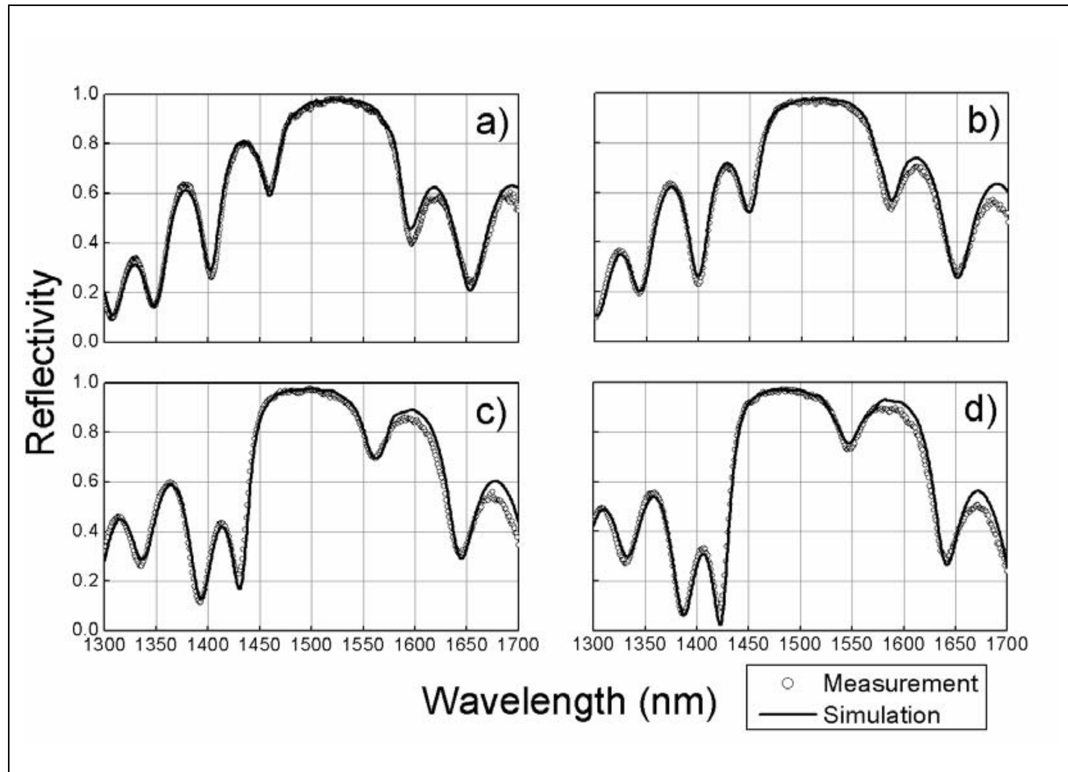

Figure 3.6: Cavity tuning of a sample by etching: a) Deviation in GaAs layers are -8.0% and in AlAs layers +4.0%. Absorption peak is around 1600 nm. b) After 20 nm surface etch, c) after 45nm more surface etch, d) after 15nm more etch, absorption peak is at 1548nm.

Table 3.2. Metallization to p+ layer is done with Ti/Au (100 / 1000 Å) since it is easy to reach low contact resistances at p+ doping of GaAs. After metallization and liftoff, samples were cleaned for rapid thermal processing (RTP.) RTP is performed at 450 ºC for 45 sec. Contact resistance was measured from test patterns, Fig. 3.7, by HP4142B Modular DC source, and found in the order of 10^{-6} Ω-cm^2, which is in the range of GaAs FET ohmic contact resistances of 0.8 - 4 x 10^{-6} Ω cm^2 [40].

Metal	Ge	Au	Ge	Au	Ni	Au
Thickness (Å)	108	102	63	236	100	2000

Table 3.1: Evaporated metals and thicknesses for n+ ohmic contacts. [35]

3.3.3 Mesa Isolation

Devices on the samples are electrically isolated from each other by mesa etching to prevent current leakage and undesired capacitive effects. Etching was performed down to ~1580 nm, at the middle of the undoped layer.

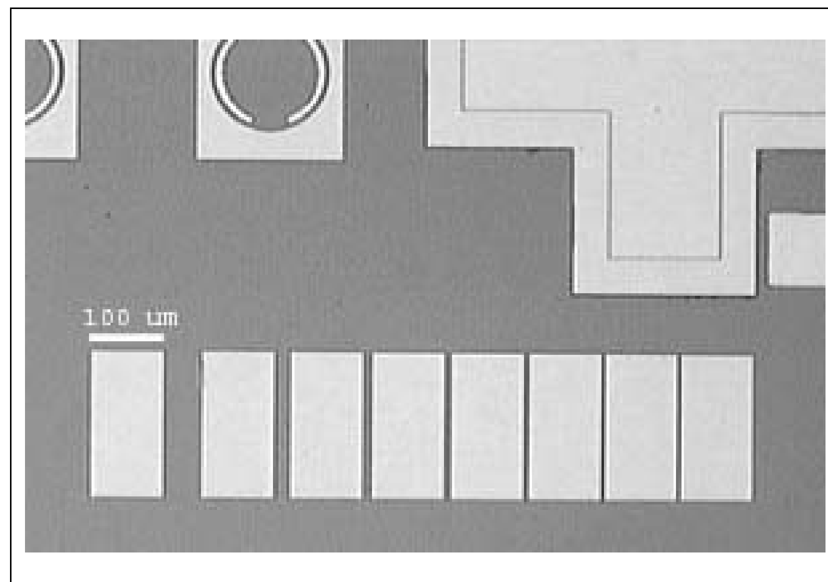

Figure 3.7: Test pattern for measuring ohmic contact resistance.

3.3.4 Dielectric Coating

Silicon nitride of thickness λ/2n, where λ is 1550 nm and n is refractive index of silicon nitride, is coated onto the sample by PECVD, for antireflection coating and passivation. Passivation includes both isolation of metals and the

active area from outside and the isolation of the device mesa sidewalls from the interconnect metals. In high-speed samples, it also behaves as the dielectric material for metal-dielectric-metal capacitors. Growth is carried out with parameters presented in Table 3.2, along with the ellipsometer, to control both refractive index (~1.76), and the thickness of the nitride film. After coating, PL is carried out and nitride is etched through openings of the resist using a HF:H_2O (1:100) solution.

3.3.5 Interconnect Metallization

In order to connect devices to transmission lines or microwave compatible pads, an interconnect metal layer was deposited over the insulating GaAs layer, touching the n+ and p+ layers and laying over nitride at the sidewalls. PL for this step is usually an image reversal PL since the liftoff step is considerably easy, as it is explained in Section 2.2.2. Au was the major component of metal with about 0.8 µm, with Ti as an adhesion promoter to the semiconductor with a thickness of ~1/10 of Au layer thickness.

3.3.6 Lift-off

After all metallization steps, elements deposited onto the resist were lifted off in acetone. Depending on the metal's thickness and development of the resist, liftoff may last from seconds up to days. Additional treatments were applied to speed up the liftoff duration, such as ultrasound, and swabbing with a Q-tip, but these have a potential of damaging devices and even the sample.

3.3.7 Airbridge Metal Formation

The high-speed process was completed with an airbridge formation, which was not included in the standart process. This is a two mask level process, including airpost formation from resist and airbridge metallization. Airbridge is needed

for low parasitic capacitance and carrying of high currents is possible in this way.

Post openings are formed with normal PL, and samples were hard-baked at 140 ºC for 30 min; so that posts do not dissolve in the following lithography. Normally, resist thickness is about 1.3 µm. It is thinned with RIE using O_2 down to 0.5 µm, so that 0.8 µm metal thickness will be enough to make the bridge. Image reversal PL is made for the next step, and 0.8 µm Ti/Au metal is deposited. When all resists are cleaned in acetone, bridge hangs in the air, with one end touching the pads and the other on the ohmic contacts, as shown in Fig. 3.9. Upper metal of MIM capacitor is also formed in bridge metallization.

p-i-n Photodetector Process Steps – 1 (Standart Process)		
Step	**Parameters**	
Cavity Tuning by Surface Etch	Etchant:	25%NH_3:H_2O_2:H_2O= 8:2.4:600 ml
	Rate:	~25 Å/sec
Photolithography	Spin:	5000 rpm x 40sec
	Dehydration Bake:	110 °C x 50 sec
	Expose:	160 mJ
	Developer:	AZ400K: H_2O=15:60 ml
	Dev. Time:	~50sec
N+ Layer Etch	Etchant:	25%NH_3:H_2O_2:H_2O= 8:2.4:300ml
	Etch Rate:	~50 Å/sec
N+ Ohmic Metallization	Metals:	Ge / Au / Ge / Au / Ni / Au
	Thickness:	108 / 102 / 63 / 236 / 100 / 2000 Å
Photolithography	Spin:	5000 rpm x 40 sec
	D. Bake:	110 °C x 50 sec
	Expose:	160 mJ
	Developer:	AZ400K: H_2O=15:60 ml
	Dev. Time:	~50sec
p+ Ohmic Metallization	Metals:	Ti / Au
	Thickness:	100 / 1000 Å
Photolithography	Spin:	5000 rpm x 40 sec
	D. Bake:	110 °C x 50 sec
	Expose:	160 mJ
	Developer:	AZ400K: H_2O=15:60 ml
	Dev. Time:	~50sec
Mesa Etch	Etchant:	25%NH_3:H_2O_2:H_2O = 8:2.4:300 ml
	Etch Rate:	~50 Å/sec
Rapid Thermal Annealing	Temp:	450 °C
	Time:	45 sec

Table 3.2: Process details for p-i-n photodetector (standart process)

Nitride (SiN_x) Coating	SiH_4:	180 sccm
	NH_3:	45 sccm
	Temp:	250 °C
	RF Power:	20 W
	Pressure:	1000 mTorr
	Growth Rate:	~128 Å/min
	Film Thickness:	λ/2n = ~1550/2x1.76
		= 440 nm
Photolithography	Spin:	5000 rpm x 40 sec
	D. Bake:	110 °C x 50 sec
	Expose:	160 mJ
	Developer:	AZ400K: H_2O=15:60 ml
	D. Time:	~50sec
Nitride Etch	Etchant:	HF: H_2O = 1:100 ml
	Rate:	~440 nm / 15sec
Photolithography	Spin:	5000 rpm x 40 sec
(Image Reversal)	D. Bake:	110 °C x 50 sec
	1st Expose:	60 mJ
	Bake:	110 °C x 2 min
	2nd Expose:	Float Exposure without mask / 160 mJ
	Developer:	AZ400K: H_2O=15:60 ml
	Dev. Time:	~50sec
Interconnect Metallization	Metals:	Ti / Au
	Thickness:	100-150 / 6900-6850 Å
Lift-off	Acetone	

Table 3.2: (cont.) Process details for p-i-n photodetector (standart process)

p-i-n Photodetector Process Steps – 2 (High Speed Process)		
Step	**Parameters**	
Cavity Tuning by Surface Etch	Etchant:	25%NH_3:H_2O_2:H_2O= 8:2.4:600 ml
	Rate:	~25 Å/sec
Photolithography	Spin:	5000 rpm x 40sec
	Dehydration Bake:	110 °C x 50 sec
	Expose:	160 mJ
	Developer:	AZ400K: H_2O=15:60 ml
	Dev. Time:	~50sec
n+ Layer Etch	Etchant:	25%NH_3:H_2O_2:H_2O= 8:2.4:300ml
	Etch Rate:	~50 Å/sec
n+ Ohmic Metallization	Metals:	Ge / Au / Ge / Au / Ni / Au
	Thickness:	108 / 102 / 63 / 236 / 100 / 2000 Å
Photolithography	Spin:	5000 rpm x 40 sec
	D. Bake:	110 °C x 50 sec
	Expose:	160 mJ
	Developer:	AZ400K: H_2O=15:60 ml
	Dev. Time:	~50sec
p+ Ohmic Metallization	Metals:	Ti / Au
	Thickness:	100 / 1000 Å
Photolithography	Spin:	5000 rpm x 40 sec
	D. Bake:	110 °C x 50 sec
	Expose:	160 mJ
	Developer:	AZ400K: H_2O=15:60 ml
	Dev. Time:	~50sec
Mesa Etch	Etchant:	25%NH_3:H_2O_2:H_2O = 8:2.4:300 ml
	Etch Rate:	~50 Å/sec
Rapid Thermal Annealing	Temp:	450 °C
	Time:	45 sec

Table 3.3: Process details for a p-i-n photodetector using high-speed process.

Photolithography	Spin:	5000 rpm x 40 sec
(Image Reversal)	D. Bake:	110 °C x 50 sec
	1st Expose:	60 mJ
	Bake:	110 °C x 2 min
	2nd Expose:	Without Mask / 160 mJ
	Development:	AZ400K: H_2O=15:60 ml
	Dev. Time:	~50sec
Interconnect Pad Metallization	Metals:	Ti / Au
	Thickness:	100-150 / 6900-6850 Å
Nitride (SiN_x) Coating	SiH_4:	180 sccm
	NH_3:	45 sccm
	Temp:	250 °C
	RF Power:	20 W
	Pressure:	1000 mTorr
	Growth Rate:	~128 Å/min
	Film Thickness:	$\lambda/2n$ = ~1550/2x1.76
		= 440 nm
Photolithography	Spin:	5000 rpm x 40 sec
	D. Bake:	110 °C x 50 sec
	Expose:	160 mJ
	Developer	AZ400K: H_2O=15:60 ml
	DevTime:	~50sec
Nitride Etch	Etchant:	HF: H_2O = 1:100 ml
	Rate:	~440 nm / 15sec

Table 3.3: (cont.) Process details for a p-i-n photodetector (high-speed process).

Photolithography for Post Openings	Spin: 5000 rpm x 40 sec D. Bake: 110 °C x 50 sec Expose: 160 mJ Development: AZ400K: H_2O=15:60 ml D. Time: ~50sec Hard Bake: 140 °C x 30 min in Resist Thickness: ~1.3 µm
Reactive Ion Etching of Photoresist for Post Openings	O_2: 20 sccm Gas Conditioning Time: 30 sec Pressure: 70 µbar RF Power: 50 W Rate: ~600-700 Å/min Resist Thickness for Posts: 0.5 µm
Photolithography (Image Reversal)	Spin: 5000 rpm x 40 sec D. Bake: 110 °C x 50 sec 1st Expose: 60 mJ Bake: 110 °C x 2 min 2nd Expose: Without Mask / 160 mJ Development: AZ400K: H_2O=15:60 ml Dev. Time: ~50sec
Air Bridge Metalization	Metals: Ti / Au Thickness: 100 Å / 7900 Å
Liftoff	Acetone.

Table 3.3: (cont.) Process details for a p-i-n photodetector (high-speed process).

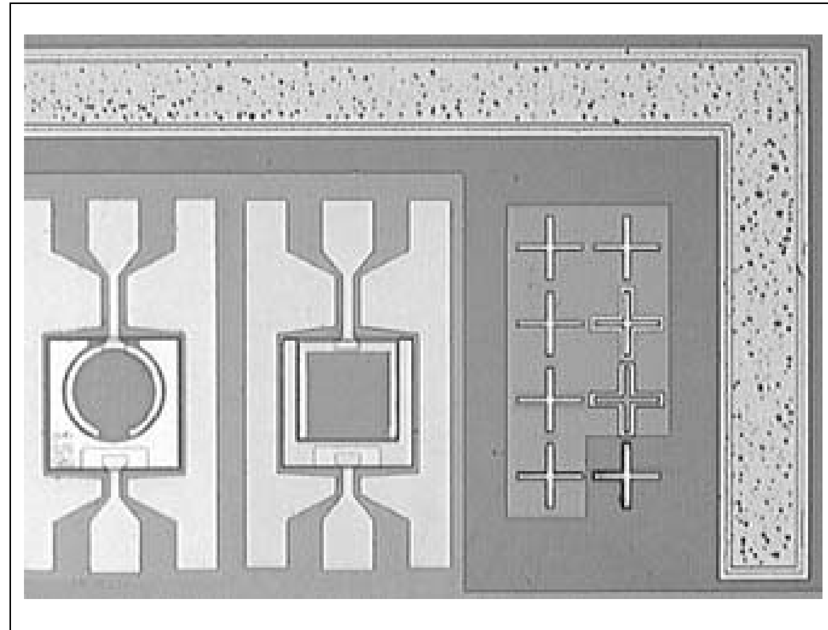

Figure 3.8: Photodetectors with quantum efficiency mask sequence. Notice the cheese-like metal surfaces of n+ ohmic contacts, which occur after RTP.

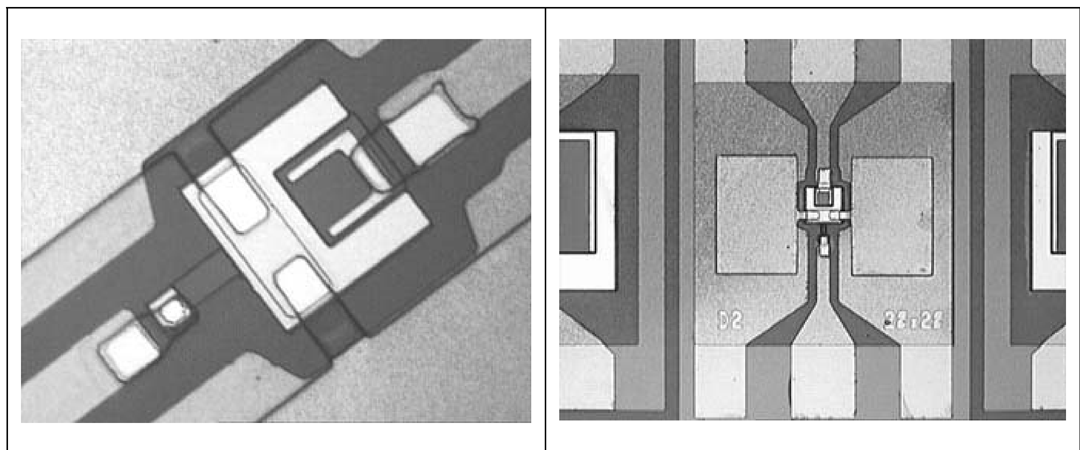

Figure 3.9: Photodetectors of 20 μm x 20 μm active area, with high-speed mask sequence. Left photograph was taken after bridge metallization PL. Areas of bridges and top MIM capacitor layers are open and the rest is with resist. Right photograph is after all steps were finished, and the dark square area is dielectric.

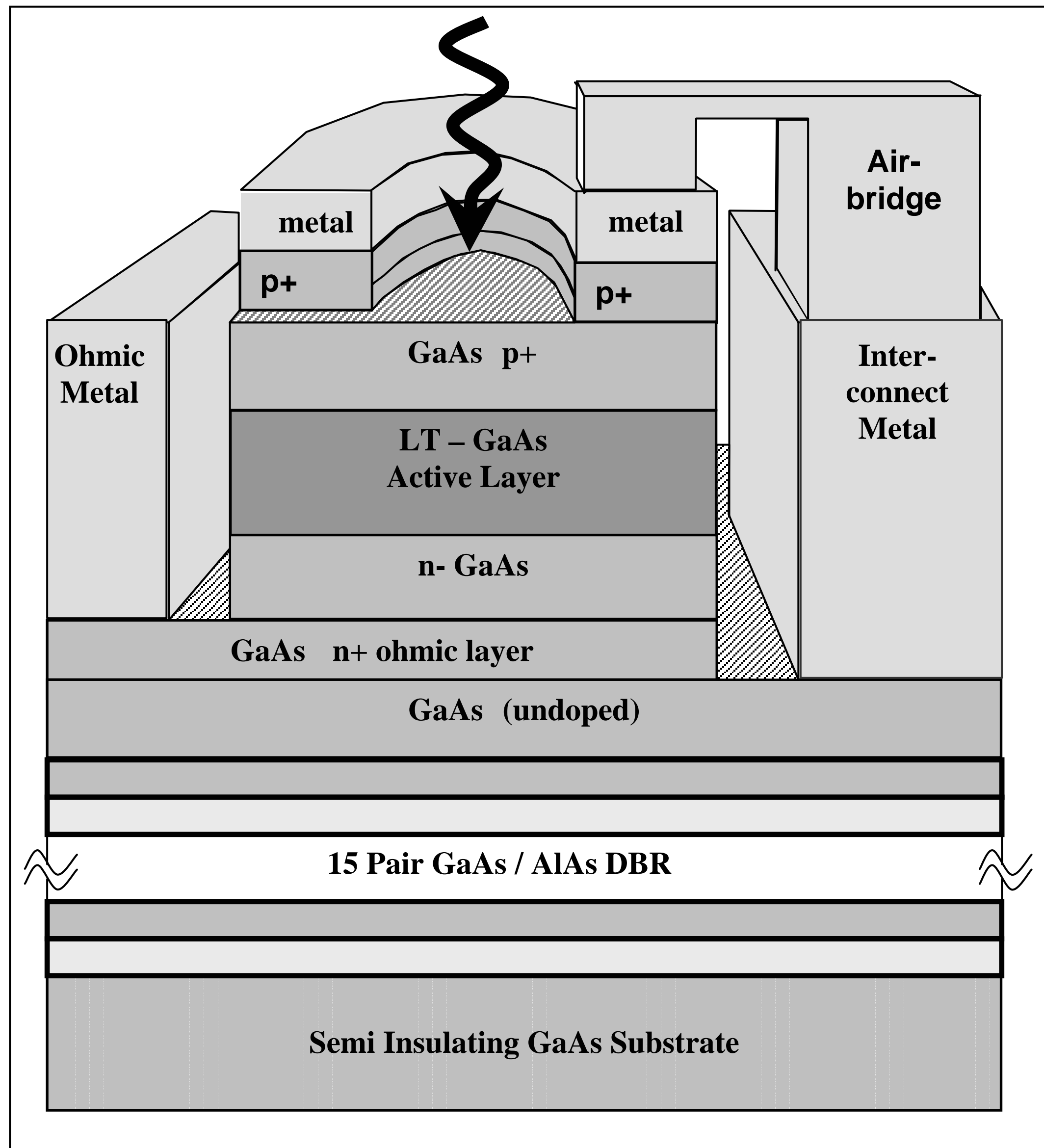

Figure 3.10: Lateral structure of the photodetector after fabrication.

Chapter 4

Measurements

In this chapter, we present the experimental results obtained from fabricated detectors. Samples from two different wafers were fabricated with two kinds of structures, namely RCE and single pass. First current -voltage (IV) measurements were made, because after this step we could learn that fabrication was at least successful and detectors show diode characteristics. Then, quantum efficiency (QE) and high-speed measurements were performed on functional devices.

4.1 Current vs. Voltage Measurements

We used an HP4142B Modular DC Source/Monitor analyzer and a probe station for IV measurement. Turn-on voltages were around 2.5 V, which is higher for a p-i-n GaAs diode. This suggests that the As clusters in LT-GaAs region acts as strong current sinks [7]. Breakdown voltages ranged from -15 V to -20 V and from -5 V to -12 V for the USA samples and Spain samples respectively. We expected much larger voltage levels, since one of the most important properties of LT-GaAs is its high breakdown field; about tenfold larger than the normally grown GaAs [37]. Possible reasons for the low breakdown field may be due to fabrication related problems. At 1V reverse bias, devices showed dark currents in the order of tens of nA. The diodes showing good IV characteristics are used in the subsequent measurements.

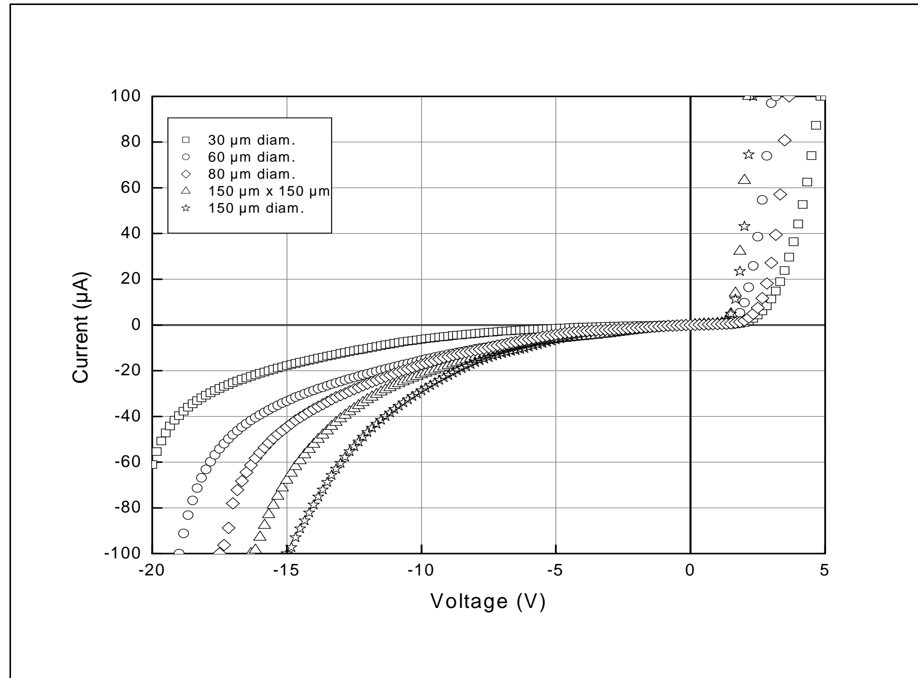

Figure 4.1: Current vs. Voltage characteristic of different size photodetectors

4.2 Quantum Efficiency Measurements

Spectral photo-response of the fabricated devices was measured in the 1500-1600 nm range using a tunable laser source and a lock-in amplifier. The output of the laser was coupled to a single-mode fiber. The light was delivered to the devices by way of a lightwave fiber probe, as shown in the diagram at Fig. 4.2, and the electrical characterization was carried out on a microwave probe station.

Figure 4.3 shows the spectral quantum efficiency measurement of a 60 µm diameter RCE photodiode as a function of applied reverse bias voltage. The

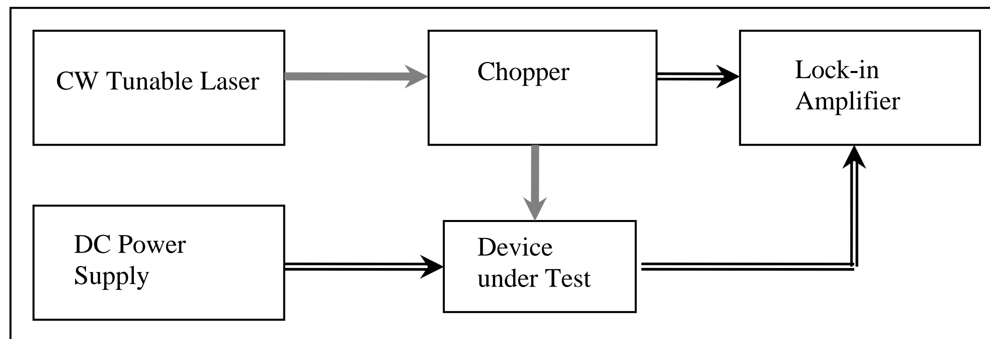

Figure 4.2: Basic schematics of quantum efficiency setup

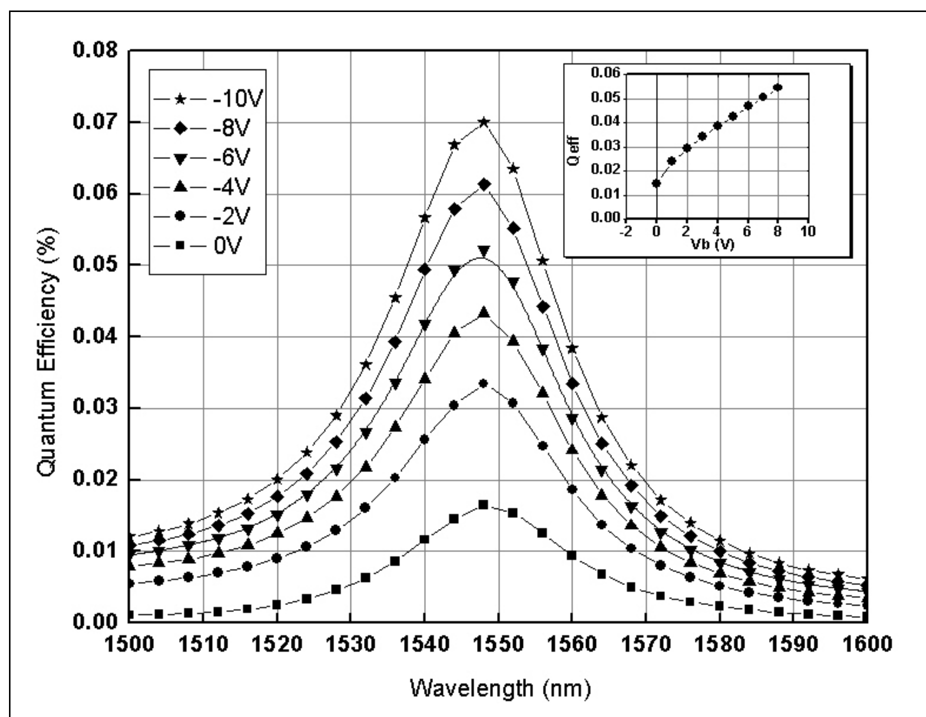

Figure 4.3: Quantum Efficiency of a 60 µm diameter device from USA wafer.

resonant peak was measured to be around 1548 nm. The peak efficiency increased with reverse bias, mainly due to the enhanced depletion of the active LT-GaAs layer. The same measurement was carried out for sample for the Spain wafer. The peak efficiency, in this case, is at 1540 nm, due to shift at the bottom mirror's reflectance spectral window. Maximum efficiencies at -3 V were 0.04% and 0.006% for the USA and Spain wafers, respectively. To compare the efficiency performance of RCE structure with the single-pass structure, single-pass devices were also measured, shown in Fig. 4.5. The same efficiency figure is measured as 0.007% for single-pass sample at 1545 nm. We observed that USA wafer produced better efficiencies than Spain wafer. This was possibly due to the differences at actual growth temperatures during the growth of LT-GaAs region, since the temperature is not measured directly, but instead from the infrared radiation from the wafer.

In the next figure (Fig. 4.6), the measured and simulated spectral quantum efficiency curves of RCE and single-pass detector samples are shown. The measurements were taken under 3 V reverse bias. The use of resonant cavity increased the quantum efficiency by a factor of 4.9. The measured enhancement factor was even higher under zero bias reaching a maximum of 7.5, which was close to the theoretically calculated value of 8.3, as shown in Table 4.1.

Despite the close agreement between the measured and calculated enhancement factors, there is a huge discrepancy between the experimental and simulated quantum efficiency values. The measured efficiency values were more than 2 orders of magnitude smaller than the theoretical ones. This result can be attributed to the ultra short carrier lifetime in the active LT-GaAs layer.

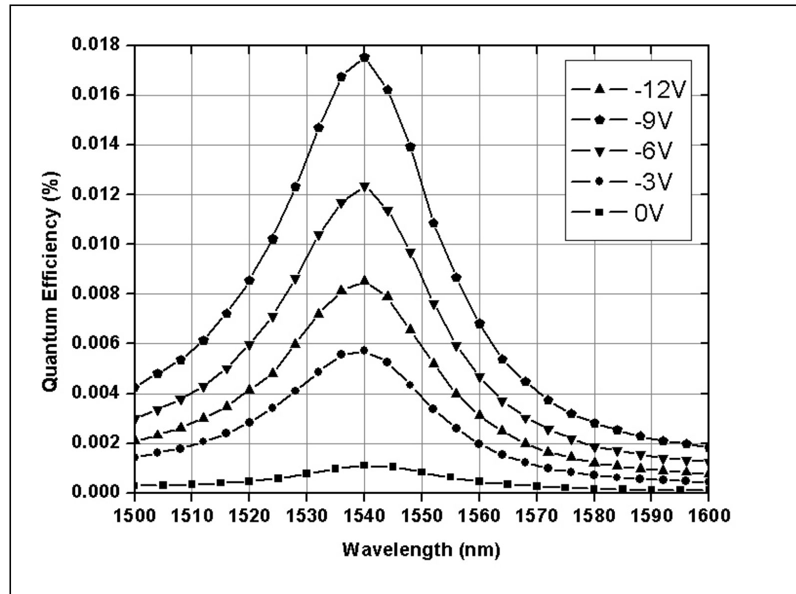

Figure 4.4: Quantum efficiency of a 60 µm diameter device from Spain wafer

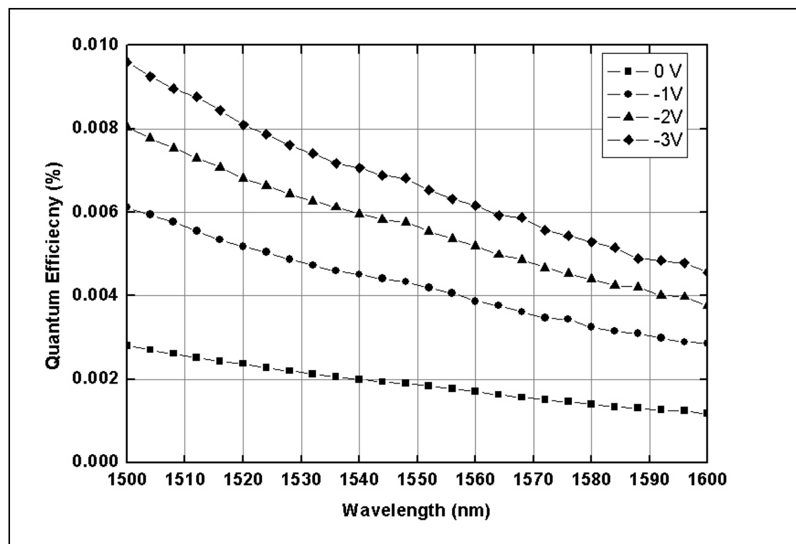

Figure 4.5: Quantum Efficiency of a single-pass device with 150 µm diameter

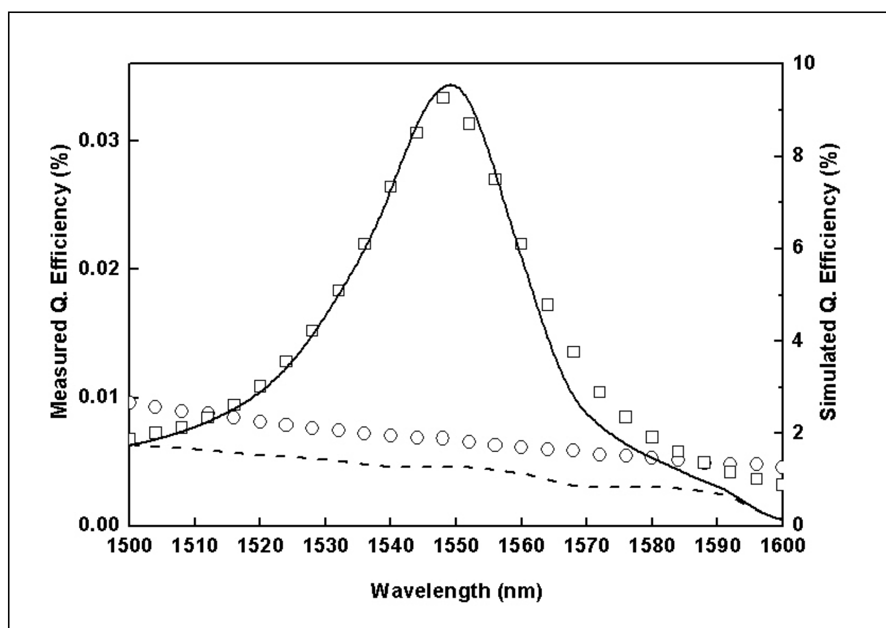

Figure 4.6: Measurement and simulation of RCE and single pass devices, of 60μm diameter. Squares: measured QE of RCE structure; circles: measured QE of single pass structure; line and dots: simulations.

With a typical carrier lifetime of ~150 fs, only the carriers that are generated very close to the edges of LT-GaAs region can survive the recombination/trapping sites and reach the p^+ or n^+ contact region. Hence, the vast majority of the photo-generated carriers within the LT-GaAs layer cannot reach the contact layers and therefore do not contribute to the photocurrent which results in poor efficiency performance. In a previous work at 1.55 μm, the external quantum efficiency was measured to be ~0.1% of a p-i-n photodetector [12]. This work does not use a RCE structure, but the wafers were annealed 10 min at 590 ºC, which strongly affects its absorption

properties [21, 36]. Therefore, low efficiencies seem to be a result of not annealing the samples after growth.

	Measurement				Simulation
	V_b=0 V	1 V	2 V	3 V	
RCE (x 10^{-4})	1.43	2.33	2.87	3.33	0.1
Single Pass (x 10^{-4})	0.19	0.43	0.58	0.68	0.012
Enhancement	7.5	5.4	5.0	4.9	8.3

Table 4.1: Peak quantum efficiencies and figures of enhancement at resonance under different bias conditions. (RCE device is 100 µm in diameter, and single-pass device is 150 µm in diameter)

4.3 High-Speed Measurements

High-speed measurements were implemented by utilizing a picosecond fiber laser operating at 1550 nm. The 1-ps full-width-at-half-maximum (FWHM) optical pulses were coupled to the active area of p-i-n photodiodes by means of a fiber probe. The resulting pulse responses were observed on a 50-GHz sampling scope.

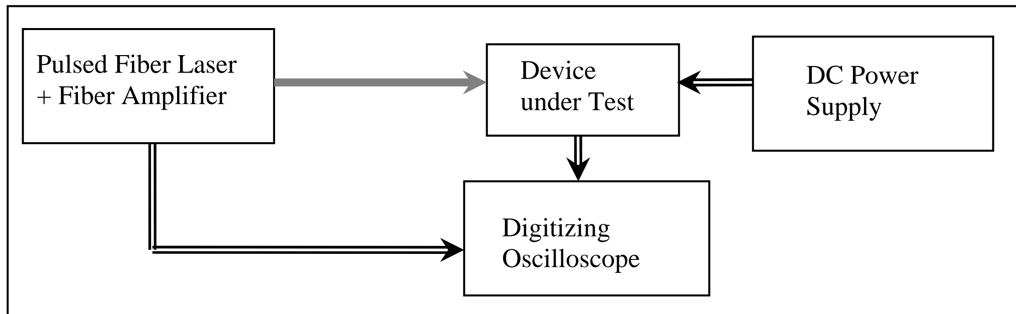

Figure 4.7: Basic schematics of high-speed setup.

Faster pulses were measured with smaller devices due to the decreased capacitance and RC time constant. The pulse response of the detectors is bias dependent. The pulse amplitude increased with reverse bias due to the enhanced device responsivity, (Fig. 4.8). However, we observed almost no change at frequency components of up to 70 GHz. FWHM of this device was calculated by Fast Fourier Transform (FFT) at around 8 GHz.

Similarly, as the devices were illuminated at higher optical power levels, stronger pulses were measured. Figure 4.9 shows the optical power dependence of the temporal high-speed response of a 7×7 μm^2 RCE photodiode under zero bias. As the optical power changed from 2.5 mW to 6.8 mW, the rise time increased from 12 ps to 16 ps. While the fall time did not change significantly (~80 ps), larger pulsewidths were measured for higher optical power levels. A minimum FWHM of 30 ps was measured at 2.5 mW illumination. The inset figure shows the corresponding FFT curves. As the temporal measurements indicated, an inverse proportionality between bandwidth and optical power was observed.

We attribute this behavior to the space-charge screening effect that becomes dominant under high optical illumination conditions [18]. A maximum 3-dB bandwidth of 11.2 GHz was obtained under 2.5 mW illumination. For optical power levels of 4, 5.5, and 6.8 mW, 3-dB bandwidths of 9.4, 8.5, and 8.3 GHz were determined respectively.

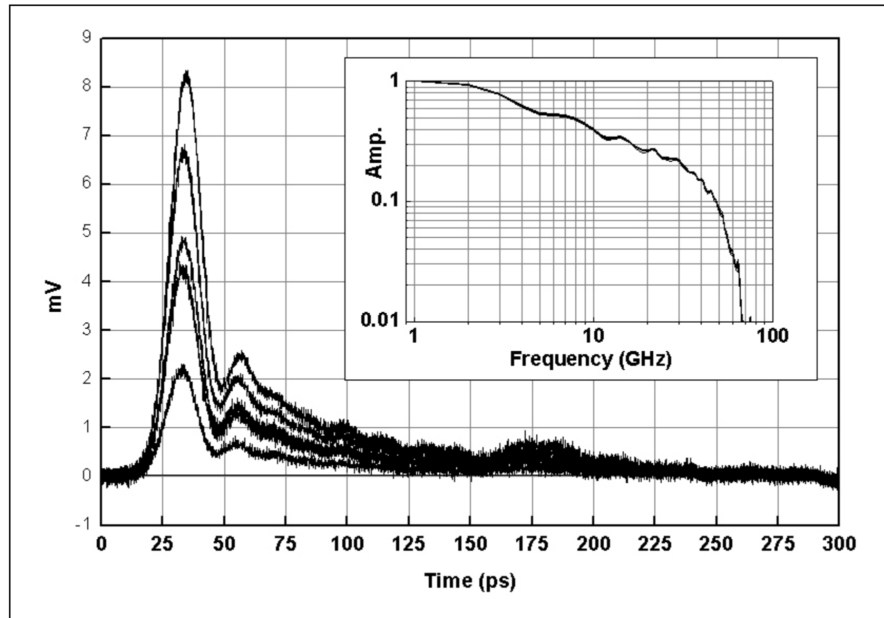

Figure 4.8: Temporal response of 30 μm device with increasing reverse bias voltage, as 1, 3, 5, 7 and 10 V.

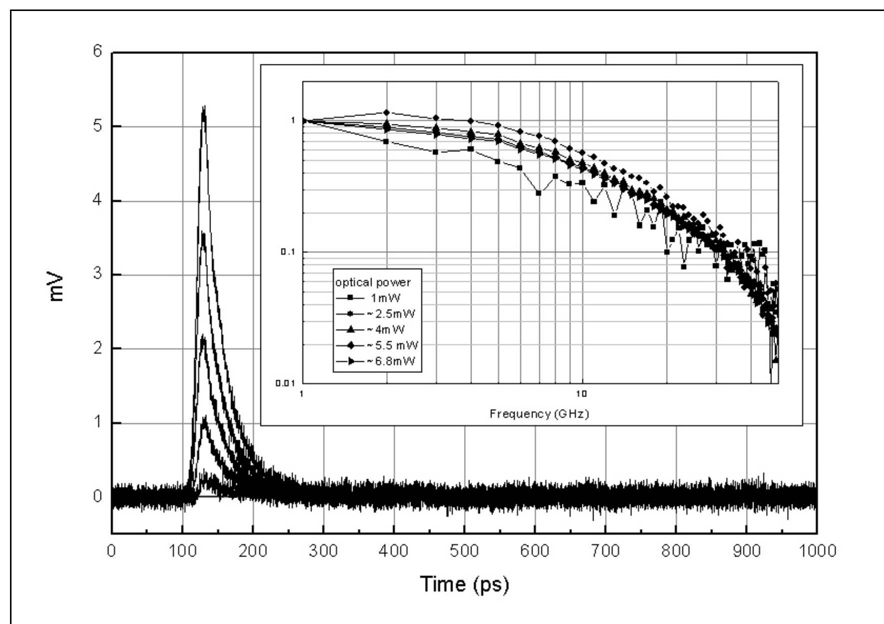

Figure 4.9: Temporal response of a 7μm x 7μm device with changing optical power illumination.

Chapter 5

Achievements and Future Directions

In the preceding chapters, we presented our work on the design, fabrication and characterization of LT-GaAs based photodetectors. For the first time, we have demonstrated a 1.55 μm high-speed operation of GaAs-based p-i-n photodiodes using LT-GaAs absorption layer and RCE detector structure. The device efficiency was enhanced by a factor of 7.5 at the resonance wavelength of 1548 nm. Temporal high-speed measurements at 1.55 μm resulted in fast pulse responses. Under low-level optical illumination, 30 ps pulse width and a corresponding 3-dB bandwidth of 11.2 GHz was achieved.

Comparing the properties of normally grown GaAs and LT-GaAs, we expected much better speed figures, and much higher breakdown voltages. Possible reasons for not achieving the expected figures of merit may be summarized as follows:

- Wafers were not post annealed after wafer growth, by which As clusters redistributed for better material structure, as was aforementioned in Section 2.1.

- Absorption region was very thick (500 nm) as compared to the distances carriers take in their lifetime. Also, the majority of carriers were absorbed far from the active region. We already saw that the absorption coefficient of LT-GaAs was more than one order of magnitude smaller. Therefore, we were not even able to completely collect the carriers generated inside the active region.

After these results, we have designed a new RCE p-i-n structure. In this design, the active region is smaller than the design mentioned in this work. Also, the electric field was maximized at the edges of the absorption region, so that a larger fraction of the photogenerated carriers would be collected before recombination. Perhaps, most importantly the wafer will be annealed at 600°C for about 10 min for the engineering of the material. Our future work will focus on the fabrication and characterization of photodetectors using this new wafer. We expect to achieve a better performance from the new devices.

Bibliography

[1] S. Donati, *Photodetectors: devices, circuits and applications*, Prentice Hall, 1999.

[2] D. A. B. Miller, "Optics for Digital Information Processing," in *Semiconductor Quantum Optoelectronics* (A. Miller, M. Ebrahimzadeh, D. M. Finlayson, eds.,) Institute of Physics and SUSSP Publ., Bristol, 1999.

[3] I. Kimukin, *Long Wavelength GaAs Based Hot Electron Photoemission Detectors*, Bilkent University M.Sc. Thesis, July 1999.

[4] K. Kato, "Ultrawide-Band/High-Frequency Photodetectors," *IEEE Trans. Microwave Theory Tech.*, vol. **47**(7), pp. 1265-1281 (1999)

[5] I. Kimukin, N. Biyikli, B. Butun, O. Aytur, S. M. Unlu, E. Ozbay, "InGaAs-Based High-Performance p-i-n Photodiodes," *IEEE Photon. Technol. Lett.*, vol. **14**(3), pp.366-368 (2002).

[6] U. K. Mishra, "Applications of GaAs Grown at Low Temperature by Molecular Beam Epitaxy," *Mat. Sci. Eng.*, vol. **B22**, pp.72-77 (1993).

[7] A. C. Warren, J. H. Burroughes, J. M. Woodall, D. T. McInturff, R. T. Hodgson, M. R. Melloch, "1.3 μm p-i-n Photodetector Using GaAs with As Precipitates (GaAs:As)," *IEEE Electron Dev. Lett.*, vol. **12**(10), pp. 527-529 (1991).

[8] R. Urata, R. Takahashi, V. A. Sabnis, D. A. B. Miller, J. S. Harris, "Ultrafast Optoelectronic Sample-and-Hold Using Low-Temperature-Grown GaAs MSM," *IEEE Photon. Technol. Lett.*, vol. **15**(5), pp. 724-726 (2003).

[9] S. Gupta, J. F. Whitaker, G. A. Mourou, "Ultrafast Carrier Dynamics in III-V Semiconductors Grown by Molecular-Beam-Epitaxy at Very Low Substrate Temperatures," *IEEE J. Quantum Electron.*, vol. **28**(10), pp. 2464-2472 (1992).

[10] J. F. Whitaker, "Optoelectronic Applications of LTMBE III-V Materials," *Mat. Sci. Eng.*, vol. **B22**, pp. 61-67 (1993).

[11] P. Grenier, J. F. Whitakes, "Subband Gap Carrier dynamics in low-temperature-grown GaAs," *Appl. Phys. Lett.*, vol. **70**(15), pp. 1998-2000 (1997).

[12] Y.-J. Chiu, S. Z. Zhang, S. B. Fleischer, J. E. Bowers, U. K. Mishra, "GaAs-Based, 1.55 μm High Speed, High Saturation Power, Low-Temperature Grown GaAs pin Photodetector," *Electron. Lett.*, vol. **34**(12), pp. 1253-1255 (1998).

[13] J.-W. Shi, Y.-H. Chen, K.-G. Gan, Y.-J. Chiu, C.-K. Sun, J. E. Bowers, "High-Speed and High-Power Performances of LTG-GaAs Based Metal-Semiconductor-Metal Traveling-Wave-Photodetectors in 1.3-μm Wavelength Regime," *IEEE Photon. Technol. Lett.*, vol. **14**(3), pp. 363-365 (2002).

[14] J.-W. Shi, K.-G. Gan, Y.-H. Chen, C.-K. Sun, Y.-J. Chiu, J. E. Bowers, "Ultrahigh-Power-Bandwidth Product and Nonlinear Photoconductance Performances of Low-Temperature-Grown GaAs-Based Metal-Semiconductor-Metal Traveling-Wave Photodetectors," *IEEE Photon.*

Technol. Lett., vol. **14**(11), pp. 1587-1589 (2002).

[15] Y.-C. Chiu, S. B. Fleischer, D. Lasaosa, J. E. Bowers, “Ultrafast (370 GHz Bandwidth) p-i-n Traveling Wave Photodetector Using Low-Temperature-Grown GaAs,” *Appl. Phys. Lett.*, vol. **79**(17), pp. 2508-2510 (1997).

[16] Y. Chen, S. Williamson, T. Brock, F. W. Smith, A. R. Calawa, “375-GHz-Bandwidth Photoconductive Detector,” *Appl. Phys. Lett.*, vol. **59**(16), pp. 1984-1986 (1991).

[17] Y.-J. Chiu, S. B. Fleicher, J. E. Bowers, “High-Speed Low-Temperature Grown GaAs p-i-n Traveling-Wave Photodetector,” *IEEE Photon. Technol. Lett.*, vol. **10**(7), pp. 1012-1014 (1998).

[18] K.-G. Gan, J.-W. Shi, Y.-H. Chen, C.-K. Sun, Y.-J. Chiu, J. E. Bowers, “Ultrahigh Power-Bandwidth-Product Performance of Low-Temperature-Grown-GaAs Based Metal-Semiconductor-Metal Traveling-Wave Photodetectors,” *Appl. Phys. Lett.*, vol. **80**(21), pp. 4054-4056 (2002).

[19] H. S. Loka, S. D. Benjamin, P. W. E. Smith, “Optical Characterization of Low-Temperature-Grown GaAs for Ultrafast All-Optical Switching Devices,” *IEEE J. Quantum Electron.*, vol. **34**(8), pp. 1426-1437 (1998).

[20] H. S. Loka, P. W. E. Smith, “Ultrafast All-Optical Switching in an Asymmetric Fabry-Perot Device Using Low-Temperature-Grown GaAs,” *IEEE Photon. Technol. Lett.*, vol. **10**(12), pp. 1733-1735 (1998).

[21] A. C. Warren, J. M. Woodall, J. L. Freeouf, D. Grischowsky, M. R. Melloch, N. Otsuka, “Arsenic Precipitates and the Semi-Insulating Properties of GaAs Buffer Layers Grown by Low-Temperature Moleacular Beam Epitaxy,” *Appl. Phys. Lett.*, vol. **57**(13), pp. 1331-

1333 (1990).

[22] H. S. Loka, S. D. Benjamin, P. W. E. Smith, "Refractive Index and Absorption Changes in Low-Temperature-Grown GaAs," *Optics Comm.*, vol. **155**, pp. 206-212 (1998).

[23] M. Y. Frankel, J. F. Whitaker, G. A. Mourou, F. W. Smith, A. R. Calawa, "High-Voltage Picosecond Switch Based on Low-Temperature-Grown GaAs," *IEEE Trans. on Electron Devices*, vol. **37**(12), pp. 2493-2498 (1990).

[24] M. S. Unlu, S. Strite, "Resonant Cavity Enhanced Photonic Devices," *Appl. Phys. Rev.*, vol. **78**(2), pp. 607-639 (1995).

[25] M. S. Unlu, M. Gokkavas, B. M. Onat, E. Ata, E. Ozbay, R. P. Mirin, K. J. Knopp, K. A. Bertness, D. H. Christensen, "High Bandwidth-Efficiecny Resonant Cavity Enhanced Schottky Photodiodes for 800-850 nm Wavelength Operation," *Appl. Phys. Lett.*, vol. **72**(21), pp. 2727-2729 (1998).

[26] E. Ozbay, I. Kimukin, N. Biyikli, O. Aytur, M. Gokkavas, G. Ulu, M. S. Unlu, R. P. Mirin, K A. Bertness, D. Christensen, "High-Speed >90% Quantum-Efficiecny p-i-n Photodiodes with a Resonance Wavelength Adjustable in the 795-835 nm Range," *Appl. Phys. Lett.*, vol. **74**(8), pp. 1072-1074 (1999).

[27] N. Biyikli, I. Kimukin, O. Aytur, M. Gokkavas, M. S. Unlu, E. Ozbay, "45-GHz Bandwidth-Efficiency Resonant-Cavity-Enhanced ITO-Schottky Photodiodes," *IEEE Photon. Technol. Lett.*, vol. **13**(7), pp. 705-707 (2001).

[28] C. Lenox, H. Nie, P. Yuan, G. Kinsey, A. L. Homles, Jr., B. G. Streetman, J. C. Campbell, "Resonant-Cavity InGaAs-InAlAs

Avalanche Photodiodes with Gain Bandwidth Product of 290 GHz," *IEEE Photon. Technol. Lett.*, vol. **11**(9), pp.1162-1164 (1999).

[29] M. S. Unlu, G. Ulu, M. Gokkavas, "Resonant Cavity Enhanced Photodetectors," in *Photodetectors and Fiber Optics* (H. S. Nalwa, ed.), Academic Press, 2001.

[30] M. Gokkavas, O. Dosunmu, M. S. Unlu, G. Ulu, R. P. Midin, D. H. Christensen, E. Ozbay, "High-Speed High-Efficiency Large-Area Resonant Cavity Enhanced p-i-n Photodiodes for Multimode Fiber Communications," *IEEE Photon. Technol. Lett.*, vol. **13**(12), pp. 1349-1351 (2001).

[31] I. Kimukin, E. Ozbay, N. Biyikli, T. Kartaloglu, O. Aytur, S. Unlu, G. Tuttle, "High-Speed GaAs-Based Resonant Cavity Enhanced 1.3 μm Photodetector," *Appl. Phys. Lett.*, vol. **77**(24), pp. 3890-3892 (2000).

[32] B. E. A. Saleh, M. C. Teich, *Fundamentals of Photonics*, John Wiley and Sons, New York, 1991.

[33] S. M. Sze, *Physics of Semiconductor Devices*, John Wiley and Sons, New York, 2nd Ed., 1981.

[34] S. K. Ghandhi, *VLSI Fabrication Principles: Silicon and Gallium Arsenide*, John Wiley and Sons, New York, 2nd Ed., 1994.

[35] E. Ozbay, *Breaking World Records in High Speed Microelectronics Using Resonant Tunneling Diodes and Schottky Photodiodes*, Stanford University Ph.D. Thesis, February 1992.

[36] F. W. Smith, "Device Applications of Low-Temperature-Grown GaAs," in *Material Research Society Symposium Proceedings, vol. 241: Low Temperature (LT) GaAs and Related Materials* (G. L. Witt, R. Calawa, U. Mishra, E. Weber, eds.), pp. 3-15 (1992).

[37] G. L. Witt, "LTMBE GaAs: Present Status and Perspectives," *Mat. Sci. Eng.*, vol. **B22**, pp. 9-15 (1993).

[38] L.F. Lester, K. C. Hwang, P. Ho, J. Mazurowski, J. M. Ballingall, John Sutliff, S. Gupta, J. Whitaker, S. L. Williamson, "Ultrafast Long-Wavelength Photodetectors Fabricated on Low-Temperature InGaAs on GaAs," *IEEE Photon. Tehnol. Lett.*, vol. **5**(5), pp. 511-514 (1993).

[39] M. Mikulics, M. Marso, P. Kordos, S. Stancek, P. Kovac, X. Zheng, S. Wu, R. Sobolewski, "Ultrafast and Highly Sensitive Photodetectors Fabricated on High-Energy Nitrogen-Implanted GaAs," *Appl. Phys. Lett.*, vol. **83**(9), pp.1719-1721 (2003).

[40] R. Williams, *Modern GaAs Processing Methods*, Artech House, Boston, 2nd Ed., 1990.

[41] B. Butun, N. Biyikli, O. Aytur, I. Kimukin, E. Ozbay, "High-Speed 1.55 µm Operation of Low-Temperature Grown GaAs Based Resonant Cavity Enhanced p-i-n Photodiodes," *submitted to Appl. Phys. Lett.* (2004).